About Meta-Lenses and Microfluidic Droplet Makers: Manipulating Matter and Optical Flows for Novel Applications

About meta-lenses and microfluidic droplet makers: Manipulating matter and optical flows for novel applications

A dissertation presented

by

Benedikt Groever

to

The Department of Enginnering and Applied Sciences

in partial fulfillment of the requirements

for the degree of Doctor of Philosophy

in the subject of

Applied Physics

Harvard University

Cambridge, Massachusetts

November 2019

Dissertation Advisor: David Weitz, Don Ingber Benedikt Groever

About meta-lenses and microfluidic droplet makers: Manipulating matter and optical flows for novel applications

Abstract

Through the advancements in semiconductor industry, it is possible to control light at the scale of the wavelength. This enables new novel applications known as meta-surfaces. I had the great honor to work with Prof. Dr. Federico Capasso on this exciting topic. Under his supervision I was able to demonstrate a meta-lens doublet in the visible region, calculate fundamentals of meta-lens imaging with substrates and demonstrate a highly efficient chiral meta-lens. While meta-surfaces are able to control optical flows, matter flows for droplet generation can be controlled by microfluidic droplet makers. I had the honor and privilege to work with Prof. Dr. Don Ingber and Prof. Dr. David Weitz on a flow focusing mircofluidic droplet maker which was motivated through a commercial need. Those four projects are the cornerstones of my Ph.D. thesis.

THE MISSION OF HARVARD COLLEGE

Harvard College adheres to the purposes for which the Charter of 1650 was granted: "The advancement of all good literature, arts, and sciences; the advancement and education of youth in all manner of good literature, arts, and sciences; and all other necessary provisions that may conduce to the education of the youth of this country." In brief: Harvard strives to create knowledge, to open the minds of students to that knowledge, and to enable students to take best advantage of their educational opportunities. To these ends, the College encourages students to respect ideas and their free expression, and to rejoice in discovery and in critical thought; to pursue excellence in a spirit of productive cooperation; and to assume responsibility for the consequences of personal actions. Harvard seeks to identify and to remove restraints on students' full participation, so that individuals may explore their capabilities and interests and may develop their full intellectual and human potential. Education at Harvard should liberate students to explore, to create, to challenge, and to lead. The support the College provides to students is a foundation upon which self-reliance and habits of lifelong learning are built: Harvard expects that the scholarship and collegiality it fosters in its students will lead them in their later lives to advance knowledge, to promote understanding, and to serve society.

Harry R. Lewis
Dean of Harvard College
February 23, 1997

To my parents Paul and Maria Groever,

and my girlfriend Serena Bouvier

Acknowledgement

I had the great honor and privilege to work with three outstanding Harvard professors. My largest gratitude goes to Federico Capasso, Don Ingber and David Weitz. Without their continuing support my Ph.D. would not have been the unique learning experience it became. Furthermore I would like to thank my coworkers and colleges for exciting scientific discussions and interactions. Those discussions helped me to shape the projects I worked on. My special thanks also goes to my third committee member Evelyn Hu, who I had the great honor of teaching for twice. Her enthusiasm for applied physics can be contagious. Last but not least I want to thank the men and women at Harvard's Center for Nanoscale Systems (CNS), at the Wyss machine shops in Longwood, Cambridge, and at the physics machine shop in Cambridge. Their expertise was tremendously helpful in realizing the experiments.

Contents

Chapter 1

High-efficiency chiral meta-lens

1.1 Summary

We present here a compact metasurface lens element that enables simultaneous and spatially separated imaging of light of opposite circular polarization states. The design overcomes a limitation of previous chiral lenses reliant on the traditional geometric phase approach by allowing for independent focusing of both circular polarizations without a 50% efficiency trade-off. We demonstrate circular polarization-dependent imaging at visible wavelengths with polarization contrast greater than 20dB and efficiencies as high as 70%.

1.2 Introduction

Polarization, a fundamental characteristic of electromagnetic radiation, is manifest in almost all optical phenomena, from reflection and transmission at an interface, scattering by small particles, and the physics of atomic transitions [2]. Polarization-dependent effects are also manifest in many areas of optical technology, notably in polarization-resolved imaging [3]. Here it has attracted significant interest, as polarization-sensitivity provides contrast enhancement. This has found application in remote-sensing [3, 4, 5], atmospheric science [5, 6, 7], medicine [6,

7, 8, 9, 10], and biological imaging [11, 12, 13, 14]. Circular polarization states are of particular interest for the acquisition of the circular component of lights polarization may not be accomplished with simple linear polarizers alone, and thus represents the most challenging aspect of polarization measurement. Moreover, circular polarizations are of particular interest because of their interaction with the chiral structures abundant in biochemistry, and hold a certain fundamental significance in physics.

One substantial drawback of polarization imaging, and polarization optics generally, is that it typically requires relatively complex optical trains, consisting of multiple beam splitters, linear polarizers, and birefringent crystal waveplates (in order to obtain information about the circular polarization content of the light) [3]. In this realm, metasurfaces represent an important new opportunity, enabling the combination of multiple optical elements into a single component. The dimensions of the individual phase-shifting elements composing a metasurface may be adjusted, allowing for exquisite control over the phase imparted on orthogonal linear polarizations. This aspect enables the design of metasurfaces which may act in a polarization-dependent fashion. Moreover, metasurfaces are also extremely compact, consisting of flat, sub-wavelength arrays of microscopic phase elements [15, 16, 17, 18], and may be fabricated in a variety of material platforms depending on the wavelength regime of interest.

In recent years, metasurfaces and diffractive optics utilizing the so-called geometric phase have emerged as novel optical elements for addressing circular polarization states [19, 20, 21]. In the most common geometric phase-based scheme,

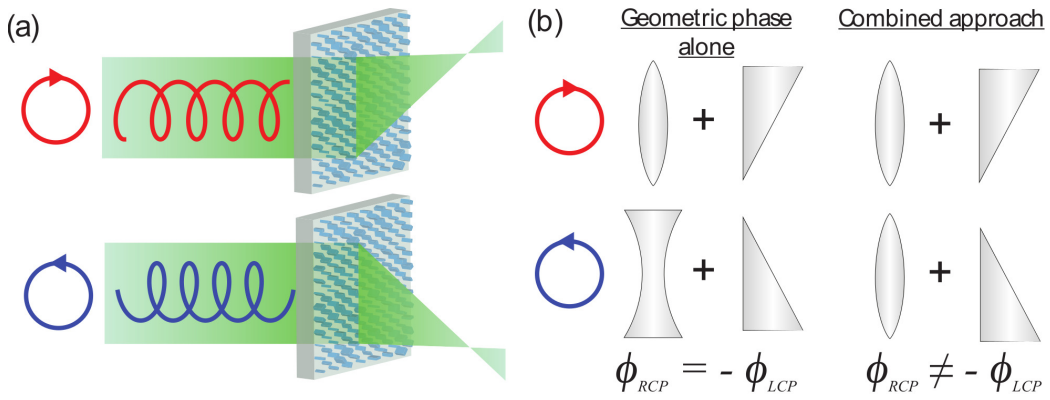

Figure 1.1: Chiral meta-lens principle. (a) Illuminated with LCP or RCP light, the meta-lens focuses an RCP - LCP image on two different positions. (b) Analogy demonstrating fundamental design differences with respect to previous chiral-lenses. A geometric phase lens designed for RCP has an equal and opposite phase profile for LCP. It focuses RCP to the right and defocus LCP to the left, here in analogy represented with a refractive lens and a wedge. The combined approach (propagation & geometric phase) allows focusing of LCP and RCP independently from each other.

a birefringent element (i.e., a half-wave plate) rotated at some angle θ causes left- and right-hand circularly polarized light to acquire equal and opposite phase shifts $\phi_{\mathrm{LCP}} = +2\theta$ and $\phi_{\mathrm{RCP}} = -2\theta$, respectively, upon interaction with the phase-shifter [22, 23, 24]. In this way, any desired phase profile may be imparted onto one circular polarization state; however, since the phase shifts are always equal and opposite, only one of the circular polarization states may be independently controlled with such a scheme.

This has some interesting and notable consequences. For example, if $\phi_{\mathrm{LCP}}(x,y)$ is a converging lens phase profile, $\phi_{\mathrm{RCP}}(x,y)$ is constrained to act as a diverging lens. This results in a 50% efficiency loss in any geometric phase device aimed at independently imaging both circular polarizations, even if two appropri-

ate geometric phase designs are interlaced [11, 25]. Moreover, the unfocused light forms an undesired background, lowering the signal-to-noise ratio of any circular polarization-discriminating measurement or image. Despite the advantage of geometric phase optical elements (such as ease of fabrication and simplicity), these effects threaten to limit their ultimate usefulness.

In the present work, we demonstrate a metasurface lens focusing each circular polarization at different angles without the above-mentioned tradeoff (Fig. 1.1a). Fig. 1.1b illustrates the merit of this approach. An off-axis lens is analogous to a superposition of the phase profiles of a lens and a wedge. If this phase profile is implemented using the geometric phase (left), one circular polarization will be focused off-axis, but when its handedness is reversed, the lens phase profile will act like a diverging lens and the slope of the wedge phase profile will change sign. Using the approach presented here, an off-axis lens may be designed truly focusing light to two off-axis positions, that is, by flipping the wedge without changing the lens from converging to diverging (right).

Our solution relies on a recently established general approach to metasurface polarization optics that does not rely on the geometric phase alone: by using a combination of geometric and propagation phases in tandem it is possible to impart fully arbitrary and independent phase profiles on the two orthogonal polarizations states [26, 27], including the two circular polarization states. This overcomes the symmetry constraint of geometric phase lenses, and a chiral lens that focusses the two polarizations in separate locations may be readily designed (Fig. 1.1a).

1.3 Design

The Jones matrix J of a linearly birefringent waveplate imparting phases ϕ^+ and ϕ^- independently on any two orthogonal input polarization states with Jones vectors $\vec{\lambda^+} = (\lambda_1^+, \lambda_2^+)$ and $\vec{\lambda^-} = (\lambda_1^-, \lambda_2^-)$ is given by:[26]

$$J = \begin{pmatrix} e^{i\phi^+}(\lambda_1^+)^* & e^{i\phi^-}(\lambda_1^-)^* \\ e^{i\phi^+}(\lambda_2^+)^* & e^{i\phi^-}(\lambda_2^-)^* \end{pmatrix} \begin{pmatrix} \lambda_1^+ & \lambda_1^- \\ \lambda_2^+ & \lambda_2^- \end{pmatrix}^{-1} \tag{1.1}$$

In the case of metasurfaces, a birefringent phase shifting element implementing J must be found. J's eigenvectors specify the angular orientation of the required element. The phases of its eigenvectors specify the phase shifts required for linear polarized light along its symmetry axes. The phase shift for linear polarization along each symmetry axis can be controlled through the geometric dimensions of each element. Geometries best matching these required phase shifts may be drawn from a library of known elements with roughly equal, high transmissivity. The above method can be understood as a unification of the propagation and geometric phases in a single element such that two independent lens profiles can be imparted. Previous designs relied on multiplexing [11, 25].

For the present chiral meta-lens, the two orthogonal polarization states are given by $\vec{\lambda_{\text{RCP}}} = \frac{1}{\sqrt{2}}(1, i)$ and $\vec{\lambda_{\text{LCP}}} = \frac{1}{\sqrt{2}}(1, -i)$. We desire to focus opposite circular polarizations to two points with equal focal lengths but equal and opposite angular displacements from the optic axis. In general, the location of the RCP and LCP foci could be fully arbitrary. The phase profiles for each polarization (Supp.

Note 1) are then given by:

$$\phi_{\mathrm{LCP}} = -\frac{2\pi}{\lambda_0}\left[\sqrt{x^2+y^2+f^2-2xf\sin\theta}-f\right] \tag{1.2}$$

$$\phi_{\mathrm{RCP}} = -\frac{2\pi}{\lambda_0}\left[\sqrt{x^2+y^2+f^2+2xf\sin\theta}-f\right] \tag{1.3}$$

Here, f denotes the desired focal length, θ denotes the off-axis angle of the lens, λ_0 is the design (free-space) wavelength, and x and y are Cartesian spatial coordinates of the lens. These phase profiles can be understood as a hyperbolic lens phase profile merged with an equal and opposite gradient term for RCP and LCP.

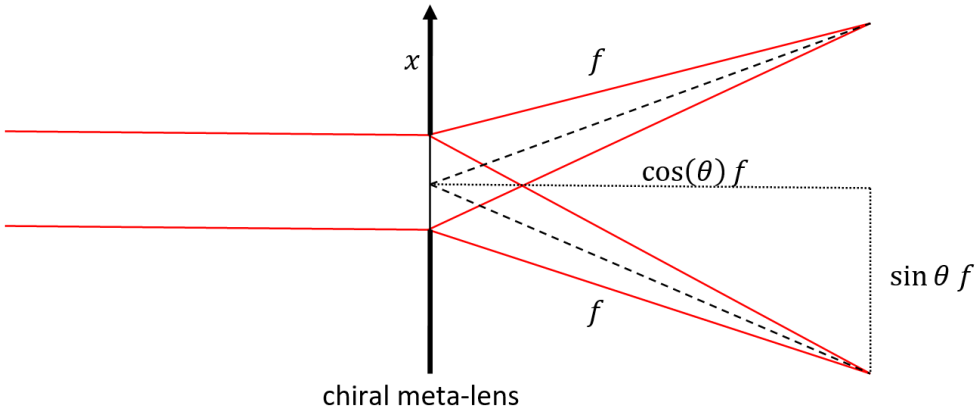

Figure 1.2: Ray diagram for chiral imaging with incident collimated light. LCP light focuses to the left. RCP light focuses to the right.

$$\varphi_{RCP} = -\frac{2\pi}{\lambda_0}\left[\sqrt{y^2 + (x + \sin\theta f)^2 + (\cos\theta f)^2} - f\right] \tag{1.4}$$

$$\varphi_{RCP} = -\frac{2\pi}{\lambda_0}\left[\sqrt{y^2 + x^2 + 2xf\sin\theta + (\sin\theta f)^2 + (\cos\theta f)^2} - f\right] \tag{1.5}$$

$$\varphi_{RCP} = -\frac{2\pi}{\lambda_0}\left[\sqrt{r^2 + 2xf\sin\theta + f^2} - f\right] \tag{1.6}$$

In this work, we implement the above design using rectangular-shaped pillar elements, fabricated in TiO_2. Neither choice is fundamental: in principle, any phase shifter geometry with two perpendicular mirror symmetry axes could suffice. TiO_2 was chosen to target the ubiquitous visible range where TiO_2 has low losses and high index, though given a proper material platform these concepts apply at any frequency.

In choosing element parameters, we draw from an FDTD-simulated library of pillars with dimensions in x and y ranging between 50 and 250nm, with a height fixed at 600nm. The variation in the dimension from 50 to 250nm provided the full phase coverage from 0 to 2π for both linear polarizations simultaneously. The pillars, fabricated on a 500 µm-thick SiO_2 substrate with a previously-reported fabrication process [28], had a 350nm nearest-neighbor separation on a hexagonal lattice. The lens is designed for λ_0 = 532nm, with f = 18 mm and $\theta = 8^\circ$. The diameter of the meta-lens as-fabricated is 1.8 mm, yielding a numerical aperture (NA) of 0.05. At such low NA, the imaging system does not need to be designed for a specific image and object distance but can still focus diffraction-limited [29]. Electron micrographs of the fabricated chiral meta-lens are shown in Fig. 1.3a-b.

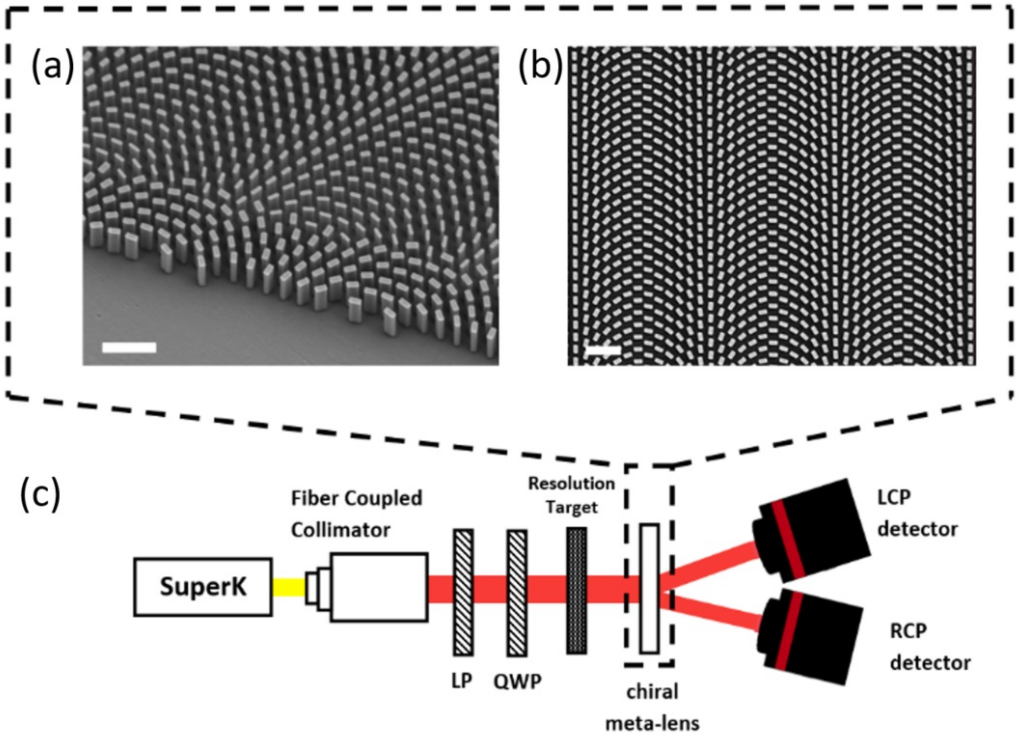

Figure 1.3: Device and measurement setup. (a) Top-side view of the SEM micrograph picture at the edge of the metasurface lens. Scale bar: 1 µm (b) Top-view SEM micrograph picture close to the center of the chiral meta-lens. Scale bar: 1 µm (c) The 1951 USAF resolution test chart illuminated with a supercontinuum laser. The polarization is controlled with a linear polarizer LP and a quarter-wave plate QWP. The sample focuses the LCP and RCP image of the resolution test chart on detector.

1.4 Characterization

In a first measurement, we sought to characterize the chiral imaging capabilities of the chiral meta-lens. A 1951 USAF resolution test chart is illuminated by a fiber-coupled super-continuum laser source whose wavelength can be varied throughout the visible range. Additionally, as depicted in Fig. 1.3c, the light passes through a linear polarizer (LP) and a broadband quarter-wave plate (QWP) before reaching the resolution target, allowing the incident polarization to be varied.

The images produced by the metasurface lens under different circular polarizations are shown in Fig. 1.4a. For linearly polarized light an equally bright image would appear on both detectors since it contains an equal proportion of LCP and RCP. The smallest bars in group 5 have a spacing and width of 8.77 µm which is larger than the diffraction limit of the chiral meta-lens: $d = \lambda_0/2NA = 5\,\mu\text{m}$. Due to the smaller size of the bars on the resolution test chart, the intensity contrast is lower. The spatial resolution along the x-axis is more sensitive to chromatic aberrations than the spatial resolution along the y-axis due to the grating term $\pm 2xf\sin\theta$ in the phase profile. This effect can be seen in the different sharpness between the horizontal and vertical bars in the image, because of the bandwidth of the super-continuum laser (10nm).

In a second measurement, we characterized the LCP - RCP focusing efficiency for different polarizations. For this measurement the resolution test target in setup Fig. 1.3b was removed, and optical power meters were placed at the LCP and RCP foci. The incident polarization is changed by rotating the QWP. The LCP -

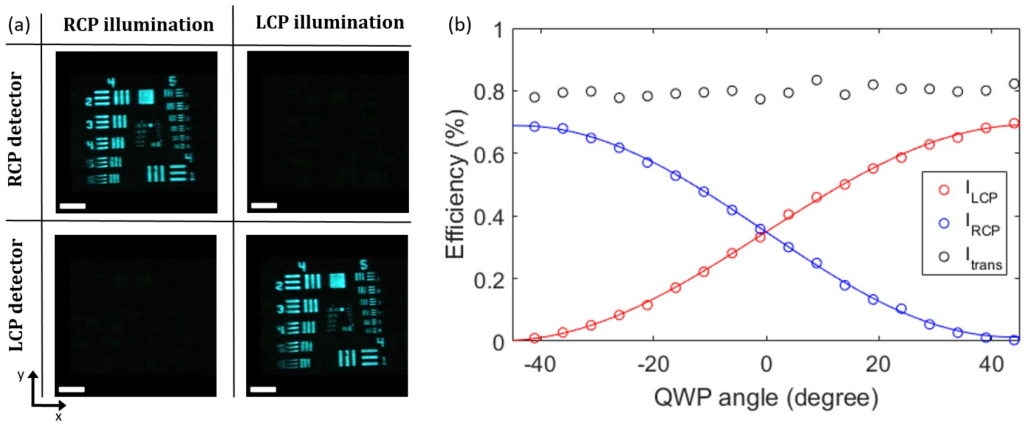

Figure 1.4: Device Performance. (a) RCP and LCP images taken of the 1951 USAF resolution test chart with the chiral meta-lens for RCP and LCP illumination at 500nm. Scale bar: 180 µm. In group 4 the bars have a spacing and width ranging from 31.25 to 17.54 µm, in group 5 from 15.63 to 8.77 µm. (b) Focusing efficiency for RCP (I_{RCP}), LCP (I_{LCP}) and transmission efficiency (I_{trans}) at different quarter wave plate (QWP) angles for 500nm illumination. The transmission efficiency through the chiral meta-lens is about 80% from which LCP and RCP have a combined focusing efficiency of 70%. Most of the remaining light couples to the 0th order while higher orders can be neglected. The data for LCP and RCP focusing efficiency is fitted with: $I_{\mathrm{RCP}} = 0.3377\sin(-0.0359\theta - 0.0065) + 0.3509$ and $I_{\mathrm{LCP}} = 0.3451\sin(-0.0334\theta + 3.1328) + 0.3463$, here θ is the QWP angle in degrees.

RCP focusing efficiency, I_{LCP} - I_{RCP}, which is defined as the ratio of the intensity in the respective focal spot over the incident intensity across the aperture of the meta-lens, was measured for various QWP angles. The QWP angle, θ, is defined as the angle between the incident linear polarization set by the polarizer and the QW plate fast axis, $\theta = 0^{\circ}$. Light incident on the chiral meta-lens is linearly polarized with vertical orientation and then focused as two beams of opposite CP and equal intensity. As $|\theta|$ increases from 0° to 45° the incident beam is elliptically polarized with varying ratios of LCP and RCP amplitudes, leading to different measured intensities by the two detectors, shown in Fig. 1.4b.

The RCP and LCP focusing efficiencies have the expected sinusoidal form with a maximum of 70%. This is significantly higher than the fundamental 50% efficiency trade-off imposed by geometric phase designs. Meta-lenses based on the geometric phase, in contrast, have been reported at a maximum focusing efficiency of 24%, owing to fundamental limits and practical constraints [11]. The transmission efficiency, I_{trans}, defined as transmitted intensity through the meta-lens over the incident intensity across the aperture of the meta-lens, was measured by bringing the power meter close to the meta-lens, so that all the diffraction orders were captured. The transmission efficiency is approximately 80% and polarization invariant. The coupling into the 0th order is also polarization insensitive and stays around 10% (Fig. 1.5). It originates from the discretization of the phase profile[30] and fabrication imperfections that affect transmission and phase.

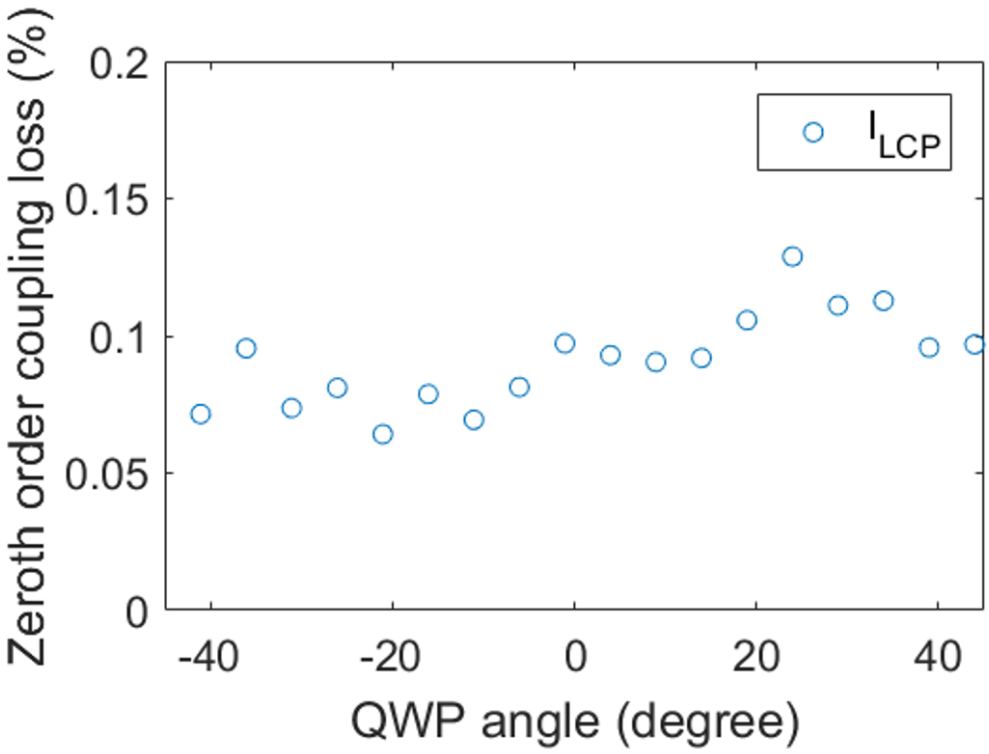

Figure 1.5: Ray diagram for chiral imaging with incident collimated light. LCP light focuses to the left. RCP light focuses to the right.

Though the lens is designed for a single wavelength, its imaging capabilities are relatively broadband (Supp. Note 4). We observe that the LCP focusing efficiency (shown in Fig. 1.6a) and the RCP focusing efficiency (Supp. Note 5) peak at 500nm. We believe this offset from the design wavelength (532nm) can be explained through fabrication imperfections in width, length and height of the nanopillars. The polarization contrast, shown in Fig. 1.6b, is defined as the intensity ratio in the RCP focal spot with RCP illumination over the intensity with LCP illumination lies within 15 to 20 dB, and similarly for the polarization contrast of LCP, limited by the detection of our photodetector.

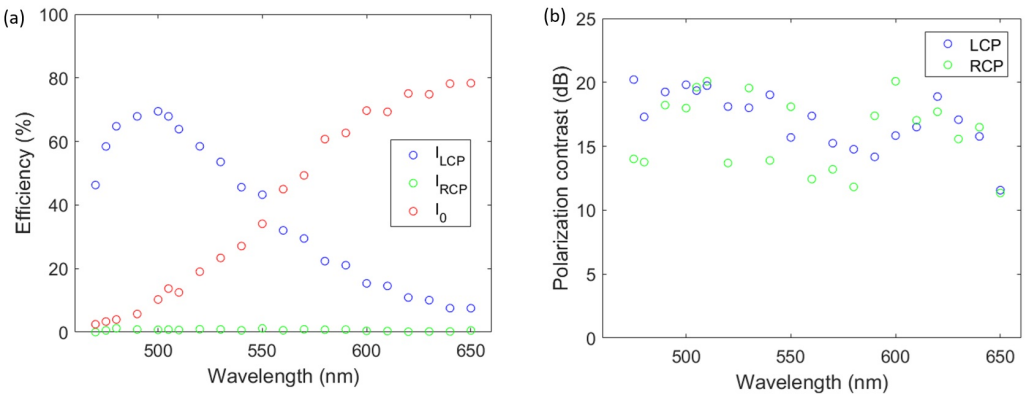

Figure 1.6: Broadband properties. (a) Focusing efficiency for LCP - RCP and 0th order coupling loss for LCP illumination at different wavelengths. The LCP focusing efficiency is peaked at 500nm. The intensity in the 0th order increases gradually from to 0% to almost 80% in the wavelength range 470nm to 650nm. (b) The polarization contrast for RCP - LCP from 470nm to 650nm.

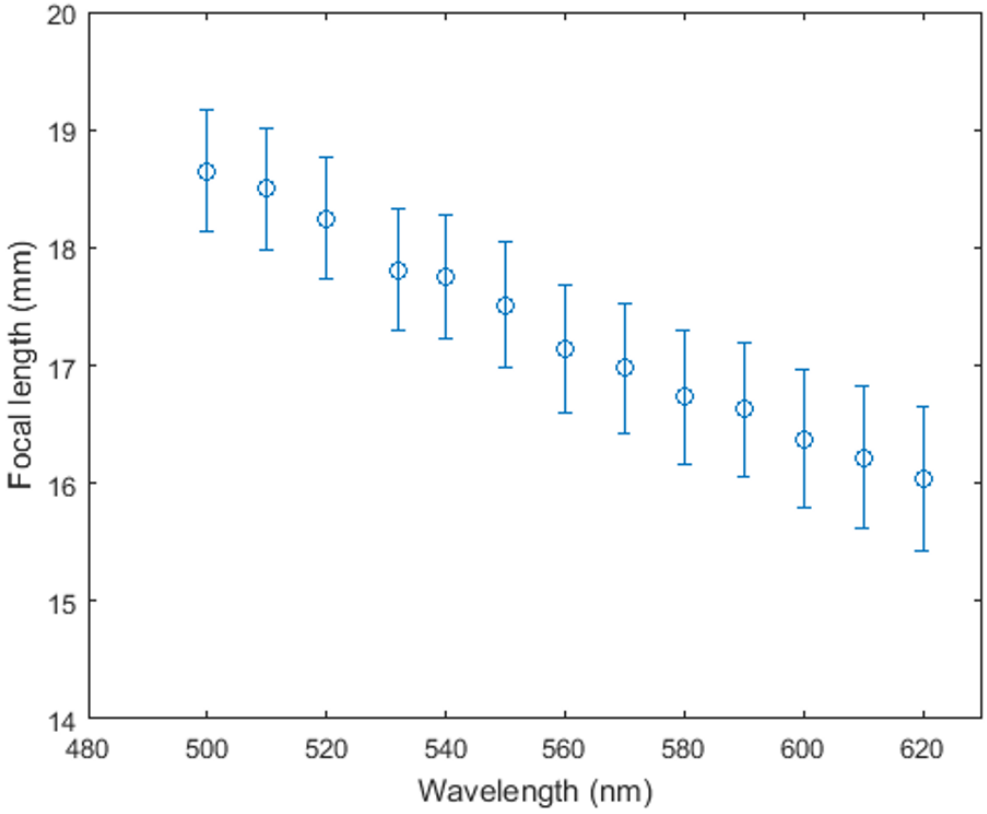

Figure 1.7: Focal length at different wavelength. The graph follows the expected behavior of a diffractive optical element: the focal length is inversely related to the wavelength. At the designed wavelength, the measured focal length is within the error of uncertainty of the designed focal length.

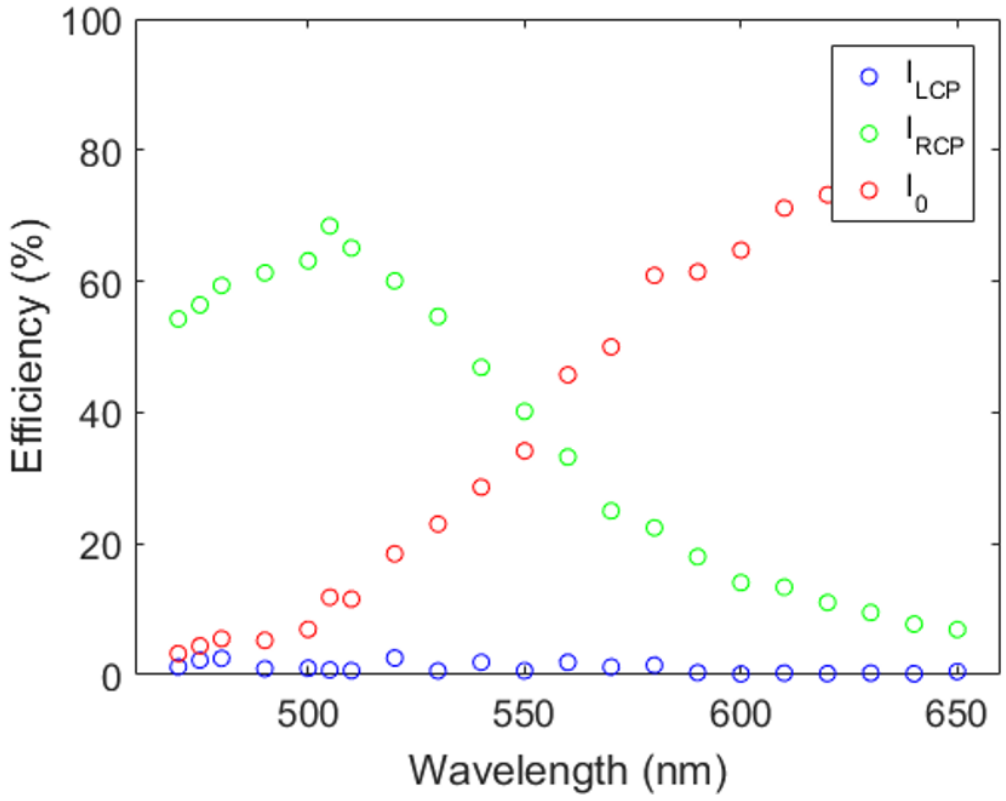

Figure 1.8: RCP focusing efficiency in analogy to the LCP focusing efficiency in Fig. 1.6(a).

1.5 Conclusion

We have presented the design and realization of a chiral meta-lens that can simultaneously and separately image both circular polarizations of a scene without suffering from the efficiency trade-off of geometric phase lenses. The design has a high polarization contrast of up to 20 dB without efficiency trade-off and thus provides the bases for a highly compact polarization imaging system for applications in remote-sensing, atmospheric science, medicine and biological imaging. The design can readily be adapted to other wavelength ranges so long as low-loss, high index subwavelength elements with tunable birefringence can be realized.

Chapter 2

Substrate aberration and correction for meta-lens imaging: an analytical approach

2.1 Summary

Meta-lenses based on flat optics enabled a fundamental shift in lens production - providing an easier manufacturing process with an increase in lens profile precision and a reduction in size and weight. Here we present an analytical approach to correct spherical aberrations caused by light propagation through the substrate by adding a substrate-corrected phase profile which differs from the original hyperbolic one. A meta-lens encoding the new phase profile would yield diffraction-limited focusing and an increase of its numerical aperture of up to 0.3 without changing the radius or the focal length. In tightly-focused laser spot applications such as direct laser lithography and laser printing a substrate-corrected meta-lens can reduce the spatial footprint of the meta-lens.

2.2 Introduction

In recent years, metasurfaces have emerged as a new way to control light through the optical properties of sub-wavelength elements patterned on the flat surface of a substrate. A sub-wavelength element can locally change the amplitude, polarization and phase of the incident electromagnetic wave to realize various optical functions in a compact configuration [17, 31, 26, 32, 33, 34]. A metasurface can

be produced through a single lithography step of nanofabrication which can easily be scaled to high-output manufacturing processes.

One of the most promising applications of metasurfaces is imaging. Here, each sub-wavelength element corresponds to one data point of the discretized phase profile of the meta-lens. Due to sub-wave- length spacing, light sees a near-continuous phase profile. During the fabrication, dimensions of the sub-wavelength elements are well controlled which enables high lens profile precision. A diffraction-limited focal spot can be achieved [35]. With conventional refractive lenses, the lens profile precision depends on the accuracy of lens curvature which is more difficult to control [36]. Future challenges of meta-lenses lay in the correction of chromatic aberrations which can be reduced by several approaches such as refractive/diffractive compound lenses [37], dispersion engineering of nanostructure resonances [38, 39] or designing a nanostructure that has control over group velocity delay and has the capability of 2π phase modulation [40, 41, 42]. This would allow circumventing the current limitations encountered in diffractive optics [43, 44, 45].

To fabricate a working meta-lens, a substrate is essential for arranging the sub-wavelength elements. But any transparent glass substrate has a refractive front surface. As of now, the refractive front surface did not play a major role in the development of meta-lenses, because most meta-lenses were designed to focus a normal incident beam [35, 46, 47]. However, in the general point-to-point imaging configuration with finite object and imaging distances, incidence is no longer normal. Refraction occurs at the front surface of the substrate, where the front

surface of the substrate is the surface with no meta-lens, which leads to spherical aberrations. In this chapter, we introduce an analytical phase profile, which corrects spherical aberrations caused by the front surface of substrate. Our approach also offers physical insight on how Seidel aberrations respond to meta-lens design changes. Previously such substrate corrections were only performed with ray-tracing techniques [48]. Without the correction of those aberrations, it is in general not possible to get diffraction-limited focusing at high numerical aperture in point-to-point imaging systems.

Besides overcoming spherical aberrations, there are also other advantages. The substrate corrected phase profile allows mounting the meta-lens on the substrate side opposing the focal spot, hence the meta-lens is better protected from outside world contaminants like dust and humidity which is important for applications in microscopy [49, 50] where the lens is close the specimen. We also find that this configuration has a higher numerical aperture and therefore a smaller diffraction-limited focal spot. This would be useful for focusing applications which require a tightly focused laser spot as direct laser lithography and laser printing [51].

Aberration correction plays a major role in the development of high resolution imaging systems for machine vision, computer vision and microscopy applications. A single, planar lens cannot produce a diffraction-limited spot along the focal plane mostly due to Petzval field curvature and coma aberration [52, 53]. Recently, a diffraction-limited meta-lens doublet along the focal plane in the visible has been demonstrated [54]. For the development of new kinds of meta-lens

objectives, ray tracing optimization is needed [54, 55]. Our analytical substrate-corrected phase profile can be used to predict better initial optimization parameters [36, 56, 57].

2.3 Hyperbolic meta-lens (HML) and substrate-corrected meta-lens (SCML)

The meta-lenses that are designed for focusing a normal incident beam which remains collimated inside the substrate are characterized by a hyperbolic phase profile [52]:

$$\varphi(\rho) = -\frac{2\pi}{\lambda_0} n_{\mathrm{m}} (\sqrt{\rho^2 + f^2} - f) \tag{2.1}$$

This formula gives the required shift at each radial coordinate to accomplish diffraction-limited focusing at the focal length f, λ_0 is the (free space) illumination wavelength and n_{m} is the refractive index of the ambient medium (n_{m} = 1). Figure 2.1a shows the ray diagram of a meta-lens with a hyperbolic phase profile mounted on a substrate, referred to as hyperbolic meta-lens (HML) hereafter. Collimated light is incident from the front surface of the substrate. The meta-lens is mounted on the other side of the substrate. The incident beam remains collimated in the substrate. The HML performs diffracted-limited focusing.

We refer to diffraction-limited focusing when all rays for a given angle of incidence intersect the optical axis at the same position. Amplitude variations of

the incoming electric field caused by absorption or reflection only need to be considered once the system is diffraction-limited as they influence the shape of the focal spot, e.g. removal of the Airy disk caused by diffraction which is known as apodization. Ray tracing is sufficient to achieve diffraction-limited focusing. Figure 2.1b shows the HML performance when collimated light is incident from the meta-lens side. Here refraction in the substrate leads to a spherically aberrated focal spot. Here, we present an analytical way to design a meta-lens to compensate for the refractive properties of the substrate so that when light is incident from the meta-lens side it enables diffraction-limited focusing as shown in Fig. 2.1d. The meta-lens with a substrate-corrected phase profile, referred to as substrate-corrected meta-lens (SCML) hereafter, has a larger phase gradient than a HML of the same focal length (Fig. 2.1c). The larger phase gradient at the edge of the SCML corrects for light propagation through the substrate. Conversely, since the SCML is designed for the light to be collimated on the meta-lens side, and if it is illuminated with collimated light from the substrate side it results in a spherically aberrated focal spot as shown in Fig. 2.1e. The fact that the HML and the SCML are diffraction-limited only for one direction of incidence is not specific to meta-lenses. Refractory plano-convex aspherical lenses, which are used to focus collimated light, have the same kind of directional behavior. In the following, we will refer to the ”wrong” configuration for each meta-lens when it is illuminated in such a way to produce a spherically aberrated focal spot; and to ”right” configuration when illumination results in a diffraction-limited spot.

The minimum achievable focal spot size for a meta-lens used in the wrong

configuration is shown in Fig. 2.1f and Fig. 2.1g respectively for the HML and the SCML. The figure of merit is the Circle of Confusion (CoC). The circle containing all incident rays is an important figure of merit for the size of the focal spot. The CoC is defined as the minimum circle, when moving along the optical axis. Images are sharpest when the image detector is at this position. As each meta-lens is only diffraction-limited for normal incidence in the right configuration, we consider only normal incidence in the wrong configuration. A rule of thumb to characterize a diffraction-limited system is to verify that all the rays fall within a disk of diameter $d_{\text{Airy}} = 1.22\ (\lambda_0/\text{NA})$, NA is the numerical aperture. d_{Airy} is roughly the diameter of the diffraction-limited Airy disk, so when this criterion is satisfied, the point-spread-function should be only modestly different from the ideal Airy pattern. The diffraction-limited Airy disk as a function of radius for the HML and SCML is shown as a shaded area in Fig. 2.1f-g. Figure 2.1f shows that the HML with a focal length of 1 mm used in the wrong configuration can still create a diffraction-limited spot if the NA is smaller than 0.3. Conversely, Fig. 2.1g shows that the SCML with a focal length of 1 mm used in the wrong configuration (i.e. collimated on the substrate side) can be diffraction-limited up to a radius of 0.25 mm, corresponding to a NA of 0.3 to 0.4 depending on the thickness of the substrate (Fig. 2.3b).

The size of the Airy disk only depends on the NA of an imaging system - not on the actual focal length or radius. When scaling the focal length and radius of the lens, the CoC scales with the same factor but the size of the Airy disk does not change. Therefore, it is harder to achieve diffraction-limited focusing with a lens

when the radius of the lens increases.

2.4 Phase profile of a diffraction-limited point-to-point focusing meta-lens

Now, we discuss the point-to-point imaging configuration. The above discussion (∞-to-f or f-to-∞) is a particular case of in which one point is at infinity. In a point-to-point imaging configuration, we need to consider an object point source located in front of the meta-lens which gets focused to an image point on the other side of the meta-lens. We call the distance from the object point source to the meta-lens the "designed front distance" d_{f} and the distance from the meta-lens to the image point the "designed back distance" d_{b}, (Fig. 2.2). The lens will work best (i.e. at the diffraction limit) when focusing light from the designed front point to the designed back point or vice versa. In the following we shall assume that the lens is operating in this way, with the object point source at the designed front position and the image point at the designed back position. If the object point source is somewhere else on the optical axis, it will still generally be focused, but the image point will have spherical aberrations. These spherical aberrations are not related to the substrate but rather are inevitable due to fix phase profile of the optical system. Their correction would require a variable imaging system, e.g. with varifocal meta-lenses [58], which can be tuned to track the object position. Such systems are widely used in cameras. To derive the phase profile of a meta-lens for diffraction-limited point-to-point focusing, we shall first consider the case

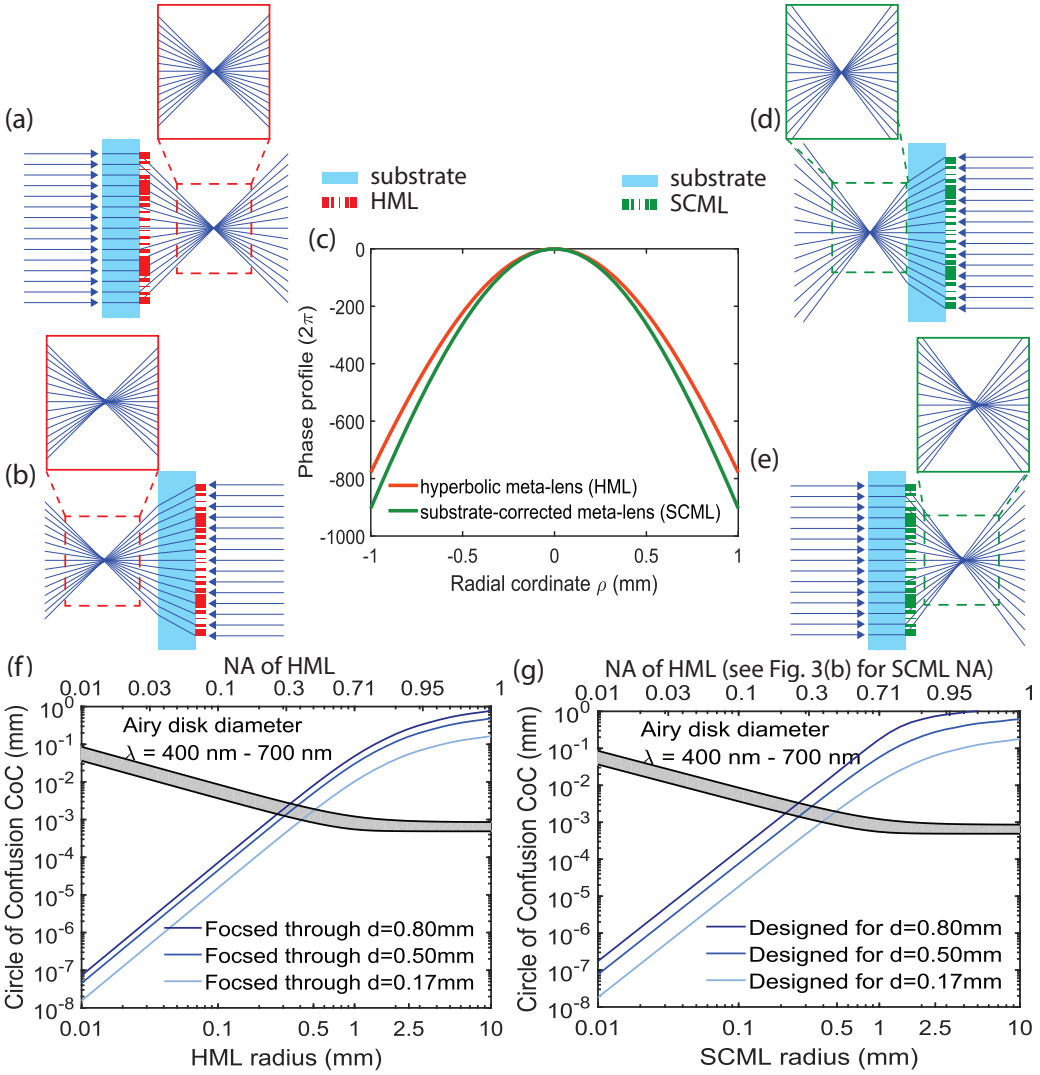

Figure 2.1: Focusing of hyperbolic meta-lens (HML) and substrate-corrected meta-lens (SCML) with incident collimated light from different sides of the substrate. (a) Ray diagram for diffraction-limited focusing with the HML. Light is incident from the front surface side of the substrate and every ray intersects the optical axis at the designed focal length. (b) Ray diagram for aberrated focusing with the HML. In this configuration where light is incident from the backside of the substrate, spherical aberration exists due to refraction at the front surface of the substrate. (c) Phase profile of the SCML and HML, Eq. (3.1) and (3.2).

Figure 2.1: (Continued)

(d) Ray diagram for diffraction-limited focusing with the SCML. Light is incident from the meta-lens side. The steeper phase profile of the SCML takes the refraction at the front surface of the substrate into account, in such a way that every ray intersects with the optical axis at the same position. (e) Ray diagram for aberrated focusing with the SCML. (f-g) CoC as a function of HML-SCML meta-lens radius, respectively, for light focused through different substrate thickness d. For all meta-lenses depicted: f = 1.0 mm, n_{sub} = 1.46, n_{m} = 1, for meta-lenses in (a-e): substrate thickness d = 0.50 mm. For meta-lenses in (c): illumination wavelength λ_0 = 532nm, the results in the other subfigures are independent of the illumination wavelength as the $1/k_0$ factor in Generalized Snell's law cancels the illumination wavelength.

of a meta-lens mounted on an infinite extended substrate $-\infty < z < 0$ as shown in Fig. 2.2a. The object point source and designed front distance are inside the substrate with a refractive index n_{sub}. The image point and designed back distance are in the ambient medium. We assume that Generalized Snell's law applies at the interface [17]:

$$\frac{1}{k_0}\frac{d\varphi}{d\rho} = n_{\mathrm{m}}\sin\beta - n_{\mathrm{sub}}\sin\alpha \tag{2.2}$$

Here, $k_0 = 2\pi/\lambda_0$, α and β are $\alpha = \arctan(\rho/d_{\mathrm{f}})$ and $\beta = \arctan(-\rho/d_{\mathrm{b}})$, respectively and $\sqrt{x^2+y^2}$ with x and y as the position coordinates on the meta-lens while the optical axis is at $x = y = 0$ along the z-direction. Generalized Snells law is valid once the height of the dielectric meta-lens is sufficiently sub-wavelength, the transmission is near unity and the separation is sub-wavelength. With the identity: $\sin(\arctan(x)) = x/(1+x^2)^{1/2}$, Eq. (2) can be written as:

$$\frac{1}{k_0}\frac{d\varphi}{d\rho} = -n_{\mathrm{m}}\frac{\rho}{\sqrt{d_{\mathrm{b}}^2+\rho^2}} - n_{\mathrm{sub}}\frac{\rho}{\sqrt{d_{\mathrm{f}}^2+\rho^2}}$$

Integration of the equation above leads to:

$$\varphi(\rho) = -k_0 n_{\mathrm{m}}\sqrt{d_{\mathrm{b}}^2+\rho^2} - k_0 n_{\mathrm{sub}}\sqrt{d_{\mathrm{f}}^2+\rho^2} \tag{2.3}$$

This is the required phase profile for diffraction-limited point-to-point focusing of a meta-lens mounted on an infinite extended substrate. In the next step,

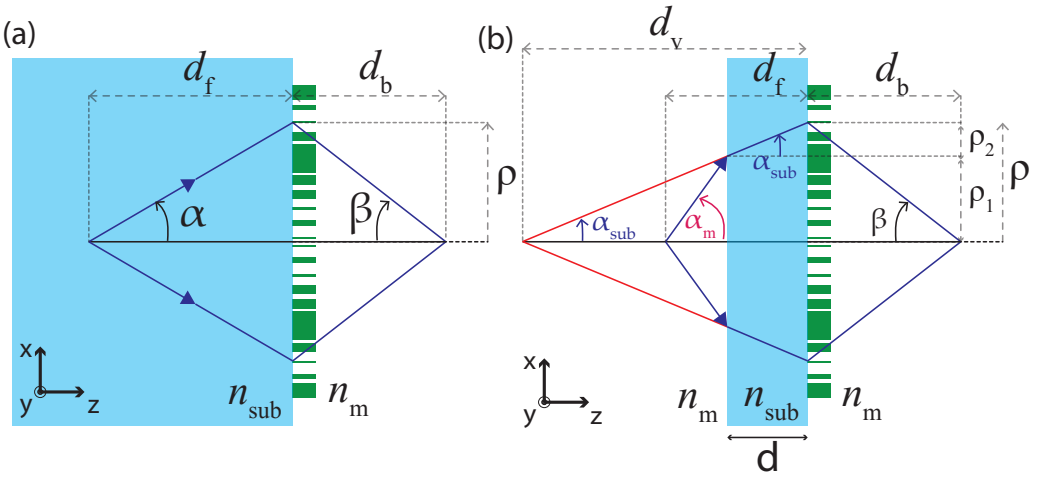

Figure 2.2: Point-to-point metasurface focusing. (a) Ray diagram of a meta-lens (dark green rectangles) mounted on an infinitely extended substrate. The image (focal spot) is inside the substrate and the object point is in the ambient medium, both on the optical axis. The designed front distance and the designed back distance are denoted as d_{f} and d_{b} respectively. (b) Ray diagram of a meta-lens mounted on a substrate of finite thickness d and object and image spots in the ambient medium. Light from a point source along the optical axis at a distance d_{f} from the meta-lens is focused to a point at distance d_{b} from the meta-lens. The distance from the intersection of the virtual rays (red lines) with the optical axis to the meta-lens is defined as virtual front distance d_{v}. The virtual front distance $d_{\mathrm{v}}(\rho)$ is a function of the radial coordinate ρ.

we assume a substrate of thickness d and $d < d_{\mathrm{f}}$. We extend virtually to the optical axis (red line in Fig. 2.2b) the rays refracted into the substrate. The distance from the intersection of the virtual ray with the optical axis to the meta-lens is the virtual front distance d_{v}. The angle in the substrate α_{sub} of the ray is given by:

$$\sin\alpha_{\mathrm{sub}} = \frac{\rho}{\sqrt{d_{\mathrm{v}}^2+\rho^2}}$$

Using Snell's law, $\sin\alpha_{\mathrm{sub}} = \sin\alpha_{\mathrm{m}} n_{\mathrm{m}}/n_{\mathrm{sub}}$, at the front surface of the substrate yields:

$$\frac{n_{\mathrm{m}}}{n_{\mathrm{sub}}}\sin\alpha_{\mathrm{m}} = \frac{\rho}{\sqrt{d_{\mathrm{v}}^2+\rho^2}}$$

Rewriting, $\sin\alpha_{\mathrm{m}}$:

$$\frac{n_{\mathrm{m}}}{n_{\mathrm{sub}}}\frac{\rho_1}{\sqrt{(d_{\mathrm{f}}-d)^2+\rho_1^2}} = \frac{\rho}{\sqrt{d_{\mathrm{v}}^2+\rho^2}}$$

ρ_1 is an axillary variable with no physical meaning, used to simplify the math. Important is the radial coordinate ρ, which is given by: $\rho = \rho_1 + \rho_2$. ρ_1 can be rewritten using similar triangles as: $\rho_1 = \rho(d_{\mathrm{v}}-d)/d_{\mathrm{v}}$. Using this identity allows rewriting the previous equation as follows:

$$\frac{n_{\mathrm{m}}}{n_{\mathrm{sub}}}\frac{\rho}{d_{\mathrm{v}}}\frac{(d_{\mathrm{v}}-d)}{\sqrt{(d_{\mathrm{f}}-d)^2+\frac{\rho^2}{d_{\mathrm{v}}^2}(d_{\mathrm{v}}-d)^2}} = \frac{\rho}{\sqrt{d_{\mathrm{v}}^2+\rho^2}}$$

It can be rewritten as a 4th order polynomial as follows:

$$d_{\mathrm{v}}^4 + a_3 d_{\mathrm{v}}^3 + a_2 d_{\mathrm{v}}^2 + a_1 d_{\mathrm{v}} + a_0 = 0 \tag{2.4}$$

where

$$a_3 = (-2d)$$
$$a_2 = (d^2 + \rho^2) - \left(\frac{n_{\mathrm{sub}}}{n_{\mathrm{m}}}\right)^2 \left(\rho^2 + (d_{\mathrm{f}} - d)^2\right)$$
$$a_1 = \left[1 - \left(\frac{n_{\mathrm{sub}}}{n_{\mathrm{m}}}\right)^2\right] \left(-2d\rho^2\right)$$
$$a_0 = \left[1 - \left(\frac{n_{\mathrm{sub}}}{n_{\mathrm{m}}}\right)^2\right] \left(d^2\rho^2\right)$$

Eq. (4) can only be solved analytically with great complication as it cannot be reduced to a lower order. The analytical solution is shown in Code File 1 (Ref. [59]). The phase gradient for diffraction-limited point-to-point focusing with a finite substrate meta-lens can be obtained by replacing the designed front distance in Eq. (2) with the virtual front distance:

$$\frac{1}{k_0}\frac{d\varphi}{d\rho} = -n_{\mathrm{m}} \frac{\rho}{\sqrt{d_{\mathrm{b}}^2 + \rho^2}} - n_{\mathrm{sub}} \frac{\rho}{\sqrt{d_{\mathrm{v}}(\rho, d_{\mathrm{f}}, d, n_{\mathrm{m}}, n_{\mathrm{sub}})^2 + \rho^2}}$$

Integration of the equation above gives:

$$\varphi(\rho) = -k_0 n_{\mathrm{m}} \sqrt{d_{\mathrm{b}}^2 + \rho^2} - k_0 n_{\mathrm{sub}} \int_0^{\rho} \frac{\rho'}{\sqrt{d_{\mathrm{v}}(\rho', d_{\mathrm{f}}, d, n_{\mathrm{m}}, n_{\mathrm{sub}})^2 + \rho'^2}} d\rho' \tag{2.5}$$

The first term of this equation is the phase profile of a HML with focal distance d_{b} and the second term is the phase profile of SCML with focal distance d_{f}. A meta-lens with the phase profile in Eq. (5) yields diffraction-limited point-to-point focusing. This is analogous to combining two aspherical lenses to a biconvex lens in refractive optics.

2.5 Numerical Aperture of HML and SCML

Consider now the phase profiles of two meta-lenses, HML and SCML with focal length f, the distance from the focal point to the meta-lens plane. Then phase profiles are given respectively by:

$$\varphi_{\mathrm{HML}}(\rho) = -k_0 n_{\mathrm{m}} \sqrt{f^2 + \rho^2} \tag{2.6}$$

$$\varphi_{\mathrm{SCML}}(\rho) = -k_0 n_{\mathrm{sub}} \int_0^{\rho} \frac{\rho'}{\sqrt{f_{\mathrm{v}}(\rho', f, d, n_{\mathrm{m}}, n_{\mathrm{sub}})^2 + \rho'^2}} d\rho' \tag{2.7}$$

Here, $f_{\mathrm{v}}(\rho', f, d, n_{\mathrm{m}}, n_{\mathrm{sub}})$ is the virtual focal length defined as the virtual front distance d_{v} by Eq. (4), $d_{\mathrm{v}} = f_{\mathrm{v}}$. The definition of the focal length f should not be mistaken with the front focal length FFL, back focal length BFL or effective focal length EFL which are different definitions of a focal length. We choose f as the focal length, because it corresponds to the best figure of merit for the spatial footprint of the whole system. The numerical aperture of SCML and HML are

given by:

$$\mathrm{NA_{HML}} = n_{\mathrm{m}} \sin\beta = n_{\mathrm{m}} \sin\left[\arctan(r/f)\right] \tag{2.8}$$

$$\mathrm{NA_{SCML}} = n_{\mathrm{m}} \sin\alpha = n_{\mathrm{sub}} \sin\alpha_{\mathrm{sub}} = n_{\mathrm{sub}} \sin\left[\arctan(r/f_{\mathrm{v}}(r))\right] \tag{2.9}$$

where NA is as usual equal to $\sin\beta$, with β the half-angle of the cone of rays converging to the image point. Here: $f_{\mathrm{v}}(r) = f_{\mathrm{v}}(r, f, d, n_{\mathrm{m}}, n_{\mathrm{sub}})$, r is the radius of the meta-lens. The NA of the SCML does not only depend on the radius and on the focal length but also on thickness and on the refractive index of the substrate. In the limit that the thickness of the substrate d approaches zero or that the refractive index ratio ($n_{\mathrm{sub}}/n_{\mathrm{m}}$) approaches unity, the NA of the SCML approaches that of the HML.

Figure 2.3a shows the NA of the SCML and the HML with a glass substrate (n_{sub} = 1.46) for different radii. As neither the SCML nor HML are immersed in a high-index liquid the NA cannot exceed a value greater than unity. The NA of all meta-lenses continuously increases to the maximum value as the radius increases. A SCML has a larger NA than a HML with the same radius and focal length. Similarly, a SCML with a thicker substrate has a NA closer to unity than a SCML with a thinner substrate. Figure 2.3b shows how much larger the NA of a SCML with different substrate thickness is compared to that of a HML, the only limit to increasing substrate thickness being the focal length (d ¡ f), to remain in a geometry corresponding to Fig. 2.2b. At large and small radii the differences in the value of the NA between the different lenses reaches zero. The maximum

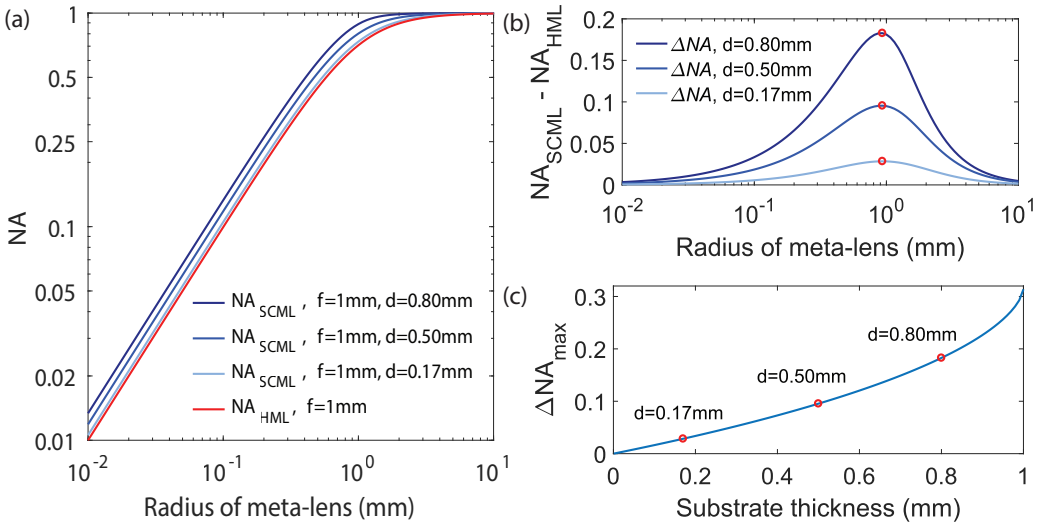

Figure 2.3: Numerical Aperture NA of substrate-corrected meta-lens (SCML) in comparison with that the of hyperbolic meta-lens (HML). (a) NA of HML for different radii and NA of SCML for different radii and substrate thicknesses d. In the limit of small substrate thickness, the NA of the SCML approaches the NA of the HML. (b) Numerical Aperture difference, $\mathrm{NA_{SCML}}$ - $\mathrm{NA_{HML}}$, ΔNA, for different radii and substrate thicknesses d. The maximum of ΔNA occurs for all SCMLs at a radius of 932.6 µm. (c) The maximum of ΔNA for different substrate thicknesses d. The points which are equivalent in subfigures (b) and (c) are marked with red circles. For all meta-lenses depicted: f = 1 mm, n_{sub} = 1.46, n_{m} = 1.

difference between the SCML and the HML for a focal length of 1 mm is reached at a radius of 932.6 µm. We verified that this is true for all substrate thicknesses up to $d = f$. The maximum difference is larger for larger substrate thicknesses as shown in Fig. 2.3c. The NA increase from a HML to SCML can be as large as 0.3, a limit set by a focal length equal to the thickness of the substrate. This enables a smaller focal spot in a more compact configuration.

2.6 Maximum angle of incidence of HML and SCML

Next, we consider off-axis illumination. Here, total internal reflection (TIR) fundamentally limits the functionality of the lens as beyond a certain angle light gets reflected instead of being focused. The maximum angle of incidence without TIR, $\theta_{\max}$ (referred to as maximum angle of incidence hereafter), is an important figure of merit as it limits the field of view and the transmission efficiency of a meta-lens. At the critical angle of TIR light travels along the meta-lens surface as shown in Fig. 2.4a [60, 61]. To calculate the critical angle, we begin by applying Generalized Snell's law at the meta-lens surface [17]:

$$n_{\mathrm{m}} \sin\theta_{\mathrm{m}} = \frac{1}{k_0}\frac{d\varphi}{d\rho}\Bigg]_{\rho=-\mathrm{r}} + n_{\mathrm{sub}} \sin\theta_{\mathrm{sub}} \tag{2.10}$$

We apply it at the lower edge of the meta-lens which is the radial coordinate ρ with the largest phase gradient. Furthermore, at the critical angle of TIR, the angle in the ambient medium is 90°, $\sin\theta_{\mathrm{m}} = 1$, and the angle in the substrate θ_{sub} can be replaced with the maximum angle of incidence by applying Snell's law at the front surface of the substrate: $n_{\mathrm{sub}} \sin\theta_{\mathrm{sub}} = n_{\mathrm{m}} \sin\theta_{\mathrm{m}}$. The phase gradient at the edge of the HML can be calculated as follows:

$$\frac{1}{k_0}\frac{d\varphi}{d\rho}\Bigg]_{\rho=-\mathrm{r}} = n_{\mathrm{m}} \frac{r}{\sqrt{f^2+r^2}} = n_{\mathrm{m}} \sin\left[\arctan\left(\frac{\mathrm{r}}{f}\right)\right] = NA$$

With equation above and Eq. (10) a criterion for the maximum angle of inci-

dence in terms of the NA of the HML and n_{m} is given:

$$\sin\theta_{\max} = \frac{n_{\mathrm{m}} - NA}{n_{\mathrm{m}}} \tag{2.11}$$

TIR at the lower edge of the HML, $\rho = -\mathrm{r}$, corresponds to $\sin\theta_{\mathrm{m}} = 1$ and an angle of incidence of $\theta_{\max}$. TIR at the upper edge of the HML, $\rho = \mathrm{r}$, corresponds to $\sin\theta_{\mathrm{m}} = -1$ and angle of incidence of $-\theta_{\max}$. In an actual meta-lens the theoretical value of the maximum angle of incidence $\theta_{\max}$ may not be achieved due to a discretization of the phase profile [17, 62], a non-zero thickness or a non-unity transmission [17]. The HML only has one possible surface for TIR as light at the front surface of the substrate goes from a lower index medium (ambient medium) into a higher index medium (substrate). For the SCML we need to consider both surfaces for TIR. As shown in Fig. 2.4b, let's first consider the surface with the meta-lens [17]:

$$n_{\mathrm{sub}}\sin\theta_{\mathrm{sub}} = \frac{1}{k_0}\frac{d\varphi}{d\rho}\Bigg]_{\rho=-\mathrm{r}} + n_{\mathrm{m}}\sin\theta_{\max}$$

The gradient term in this equation is equal to the NA of the SCML. If this surface has TIR: $\sin\theta_{\mathrm{sub}} = \pm 1$, then the criterion for the maximum angle of incidence at the meta-lens surface is given by:

$$\sin\theta_{\max} = \frac{n_{\mathrm{sub}} - NA(r, f, d, n_{\mathrm{sub}}, n_{\mathrm{m}})}{n_{\mathrm{m}}} \tag{2.12}$$

This criterion can only be fulfilled if: $\sin\theta_{\max} < 1$ and hence: NA $\geq |n_{\mathrm{sub}} - n_{\mathrm{m}}|$, otherwise the phase gradient at the edge of the meta-lens is too small to

exhibit TIR.

Now, let's consider TIR at the refractive front surface of the substrate shown in Fig. 2.4c. TIR occurs at this surface when $\sin\theta_{\mathrm{m}} = 1$, hence $\sin\theta_{\mathrm{sub}} = n_{\mathrm{m}}/n_{\mathrm{sub}}$. Substituting this relation into Eq. (10), eliminates n_{sub}. The following criterion for the maximum angle of incidence can be obtained:

$$\sin\theta_{\max} = \frac{n_{\mathrm{m}} - NA(r, f, d, n_{\mathrm{sub}}, n_{\mathrm{m}})}{n_{\mathrm{m}}} \tag{2.13}$$

This constraint for the SCML max. angle of incidence is that of an HML with the same NA. As the refractive index of the substrate is larger than that of ambient medium, TIR occurs first at the front surface of the substrate, then at the SCML surface, hence Eq. (13) is a stricter criterion for the maximum angle of incidence than Eq. (12).

Figure 2.4d shows the maximum angle of incidence for the HML and SCML for different meta-lens radii and substrate thicknesses when the focal length is 1 mm. SCMLs with a thicker substrate and larger radius (and hence a higher NA) have a smaller maximum angle of incidence than an HML with equivalent radius and focal length. Figure 2.4e shows the maximum angle of incidence for different substrate thicknesses when the radius and the focal length are both 1 mm. As the thickness of the substrate increases the maximum angle of incidence is reduced. This analysis is particularly interesting in the design of meta-lens stacking that can correct off-axis aberrations.

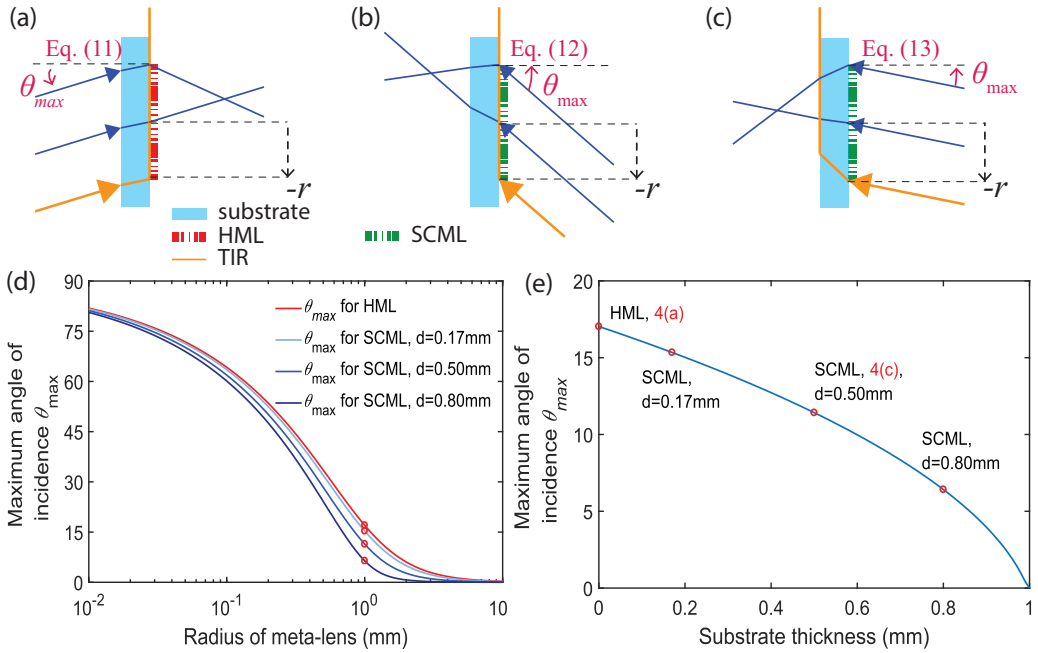

Figure 2.4: Total internal reflection (TIR) limitation for the maximum angle of incidence of hyperbolic meta-lens (HML) and substrate-corrected meta-lens (SCML). When TIR occurs, light propagates along the meta-lens and consequently limits the maximum angle of incidence. (a) Critical angle of TIR for the marginal ray (orange) at the lower edge of a HML (maximum angle of incidence $\theta_{\max}$, $\theta_{\max} = 17.03°$). When increasing the angle of incidence rays closer to the center of the meta-lens would be totally internally reflected further. (b) Critical angle of TIR at the meta-lens surface for the marginal ray at the lower edge of a SCML ($\theta_{\max} = 40.15°$). (c) Critical angle of TIR at front surface of the substrate for the marginal ray at the lower edge of a SCML ($\theta_{\max} = 11.42°$). The critical angle of TIR at the front surface of the substrate is always smaller than at the meta-lens and hence is a stricter constraint for maximum angle of incidence for the SCML. (d) Maximum angle of incidence of the HML and the SCML for different radii. The red circles have a corresponding data point in subfigure (e) - same radius and substrate thickness. (e) Maximum angle of incidence of SCML for different substrate thicknesses d. For all meta-lenses depicted: $f = 1$ mm, $n_{\text{sub}} = 1.46$, $n_{\text{m}} = 1$, for meta-lenses in (a-c): $r = 1$ mm, substrate thickness $d = 0.50$ mm, for meta-lenses in (e): $r = 1$ mm.

2.7 Seidel aberrations of HML and SCML

If the HML and SCML are used in the correct configuration, Fig. 2.1a and Fig. 2.1c respectively, spherical aberrations are not present. But besides spherical aberrations, there are 4 others monochromatic aberrations: distortion, coma aberration, Petzval field curvature and astigmatism. All 5 monochromatic aberrations are known as Seidel aberrations. Because of symmetry, astigmatism is not present in a radial symmetric optical system which is infinity-corrected. Therefore, astigmatism is neither present in the HMLs nor in the SCMLs. Coma aberration, Petzval field curvature and distortion are all present in singlet lenses both in conventional refractive lenses and in single-layer meta-lenses. For meta-lenses, this is due to the fact, that the phases profile to achieve diffraction-limited imaging depends on the angle of incidence. Angle-multiplexed phase profiles which are fully independent can only be implemented through multi-layered structures [63] as they provide enough degrees of freedom.

Coma aberration is best known for its resulting comet-shaped image, when observing an off-axis point source. In ray optics, it is defined in terms of the radial coordinate ρ at a given angle of incidence. The magnitude of coma is quantified by the distance from the chief ray to the intersection of two marginal rays, in a plane perpendicular to the optical axis. The two marginal rays have the same angle of incidence as the chief ray and hit the meta-lens plane at coordinates $\pm\rho$ [64](see Fig. 2.5a-b and Fig. 2.5c-d for the HML and SCML respectively). As the angle of incidence increases, so does the magnitude of coma, and TIR

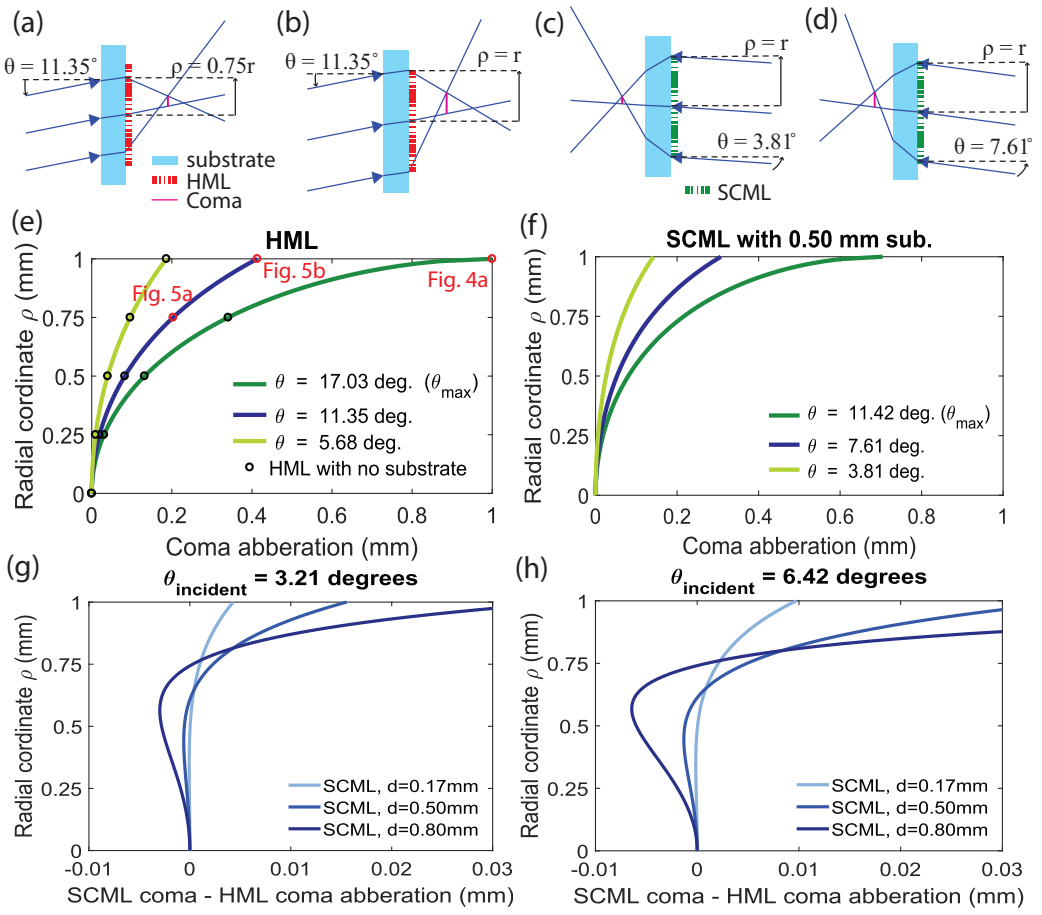

Figure 2.5: Coma aberration for hyperbolic meta-lens (HML) and substrate corrected meta-lens (SCML). Coma is a function of the radial coordinate ρ and angles of incidence θ. (a-b) Ray diagram for coma of HML at an angle of incidence θ = 11.35° for radial coordinates ρ = 0.75r and ρ = r, (a) and (b) respectively. (c-d) Ray diagram for coma of the marginal rays at the edge of a SCML for angles of incidence θ = 3.81° and θ = 7.61°, (c) and (d) respectively. The magnitude of coma is smaller for smaller angles of incidence and smaller radial coordinates. (e) Coma of the HML as a function of radial coordinate for different angles of incidence with and without substrate. The red dots indicate the corresponding ray diagram. The magnitude of coma at the edge of the HML is equal to the radius, Fig. 1.6a. (f) Coma as a function of the radial coordinate for different angles of incidence for the SCML.

Figure 2.5: (Continued)

(g-h) Coma difference between the SCML and the HML for different substrate thicknesses d at an angle of incidence of $\theta = 3.21^\circ$ and $\theta = 6.42^\circ$ for (g) and (h) respectively. $\theta = 6.42^\circ$ is the maximum angle of incidence for the SCML with a 0.80 mm thick substrate. For all meta-lenses depicted: f = 1.0 mm, r = 1.0 mm, $n_{\text{sub}} = 1.46$, $n_{\text{m}} = 1$, for meta-lenses in (a-e): substrate thickness d = 0.50 mm.

is eventually encountered. We computed the magnitude of coma for different substrates and angles of incidence with a custom-made ray tracing code. The magnitude of coma is smaller for smaller angles of incidence and smaller radical coordinates. As a direct consequence of this observation, meta-lenses with lower NA exhibit less coma than meta-lenses with a larger NA.

Figure 2.5e shows coma for the HML. We noticed that the HML has the same magnitude of coma as a meta-lens with no substrate. This is true as smaller angles in the substrate of the HML are compensated by the larger refractive index of the substrate (Generalized Snell's law). For the same reason, coma of the HML is independent of the substrate thickness. Here, a meta-lens with no substrate is considered as a theoretical limit of the finite substrate thickness case in the limit where the thickness goes to zero. At the maximum angle of incidence when TIR occurs, the magnitude of coma for marginal rays at the edge of the HML is equal to the radius of the HML (ray diagram: Fig. 2.4a).

Figure 2.5f shows coma for the SCML. For the SCML, the maximum coma is smaller than the radius of the SCML due to the TIR limitation at the front surface of the substrate (ray diagram: Fig. 2.4c). For larger substrates, this effect occurs at smaller angles of incidence and therefore leads to smaller coma. Figure 2.5g-h

show the difference in coma between the HML and the SCML at two different angles of incidence. The SCML has less coma than the HML when the radial coordinate is small. As the radial coordinate increases, this behavior is reversed. This effect is even larger when the substrate thickness is increased.

Figure 2.6a-d show the ray diagram for Petzval field curvature and distortion of the HML and the SCML with different substrate thicknesses. Petzval field curvature and distortion are defined by the focusing position of an oblique incident chief ray. The focusing position is defined as the intersection of two chief rays crossing the meta-lens plane at positions $\pm\varepsilon$.

Petzval field curvature is the distance along the optical axis from the focusing position to the flat vertical plane as ε approaches zero [64]. Imaging sensors like CMOS and CDD are flat; therefore, the focal point before the flat vertical plane causes an aberrated focal spot on the imaging sensor. Intuitively, distortion is the change in magnification across an image [64]. It is defined as the relative difference of the actual image height to the predicted image height:

$$\text{Distortion}(\%) = \left(\frac{h_\text{a} - h_\text{p}}{h_\text{a}}\right) \cdot 100 \tag{2.14}$$

Here, h_a is the actual image height, h_p is the predicted image height. The actual image height h_a is the height of the focusing position of the two chief rays. For a given angle of incidence θ, the predicted image height is the extrapolated image height from the image center: $h_\text{p} = \gamma_0 \tan(\theta)$ with:

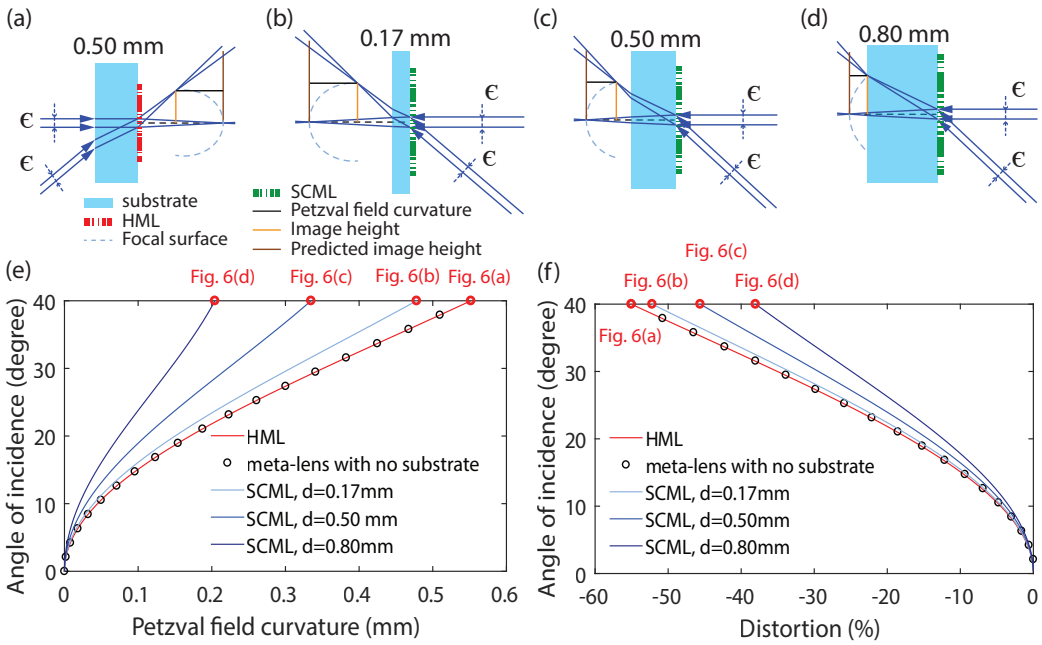

Figure 2.6: Petzval field curvature and distortion of hyperbolic meta-lens (HML) and substrate-corrected meta-lens (SCML). (a-d) Ray diagram of two chief rays for the HML and SCML with different substrate thicknesses d. When ϵ is very small the intersection of those two chief rays defines the curved focal "plane", which deviates from the flat vertical plane (blue dashed line). (e) Petzval field curvature of meta-lenses depicted in (a-d). Petzval field curvature for a certain angle of incidence is defined as the focal length shift parallel to the optical axis. Reference is normal incidence. The red dots indicate the corresponding ray diagram. (f) Distortion of the same meta-lenses. Distortion is defined as the relative difference of the actual image height to the predicted image height, Eq. (14). The predicted image height is the linear extrapolation of the image height at the center with γ_0 as proportionality constant. For all meta-lenses depicted: $f = 1$ mm, $r = 1$ mm, $n_{\text{sub}} = 1.46$, $n_{\text{m}} = 1$, for meta-lenses in (a-d): angle of incidence $\theta = 0°$ and $\theta = 40°$.

$$\gamma_0 = f - d\left(\frac{n_{\text{sub}} - n_{\text{m}}}{n_{\text{m}}}\right) \tag{2.15}$$

For an imaging system with working distance d_{f}, γ_0 is related to the image

center magnification M_0 as follows: $M_0 = \gamma_0/d_f$. For most applications distortion is not a limitation as it can be corrected with post-processing techniques. Figure 2.6e-f show that Petzval field curvature and distortion are smaller for the SCML than they are for the HML. A larger substrate thickness decreases both Petzval field curvature and distortion. At an angle of 40° incidence Petzval field curvature of the SCML with a 0.80 mm substrate is almost 3 times smaller compared to that of the HML. The HML and meta-lens with no substrate are equivalent in terms of Petzval field curvature and distortion as smaller angles in the substrate of the HML are compensated with a larger refractive index of the substrate-just as previously with coma.

2.8 Conclusion

To conclude, the SCML exhibits certain advantages over the HML. The higher NA enables a smaller diffraction-limit in a more compact configuration; monochromatic aberrations like Petzval field curvature and distortion are reduced. The higher NA of the SCML comes at the cost of a smaller maximum angle of incidence. In microscopy, the meta-lens nanostructures are better protected in the SCML configuration from outside world contaminants like dust and humidity because of the small proximity to the specimen. In immersion microscopy, the SCML would allow designing the meta-lens in air and not in a liquid [65]. With dielectric metasurfaces this is easier because of the larger index contrast. More generally, our work provides an intuitive platform towards designing meta-lens

stacking, similar to the approach that has been developed by lens makers for bulky optical components, to systematically reduce aberrations and thus give a new impulse to applications of meta-lenses in the industry [66].

Chapter 3

Meta-lens doublet in the visible

3.1 Abstract

Recently, developments in meta-surfaces have allowed for the possibility of a fundamental shift in lens manufacturing - from the century-old grinding technology to nanofabrication opening a way toward mass producible high-end meta-lenses. Inspired by early camera lenses and to overcome the aberrations of planar single-layered meta-lenses, we demonstrate a compact meta-lens doublet by patterning two metasurfaces on both sides of a substrate. This meta-lens doublet has a numerical aperture of 0.44, a focal length of 342.5 μm, and a field of view of 50° that enables diffraction-limited monochromatic imaging along the focal plane at wavelength of 532nm. The compact design has various imaging applications in microscopy, machine vision and computer vision.

3.2 Introduction

Even though ancient Greece had primitive singlet lenses, it was not until the 16th century in Holland, that for the first time two different lenses were combined to image an object [67]. A singlet planar lens cannot achieve diffraction-limited focusing for different angles of incidence [68]. This can be solved by adding lenses, and therefore provide more degrees of freedom to correct for spherical aberration,

coma aberration, astigmatism, and Petzval field curvature [69, 70]. However, this solution, combined with conventional lens manufacturing techniques, results in bulky imaging systems. In recent years, metasurfaces have emerged as a new way of controlling light through the optical properties of sub-wavelength structures patterned on a flat surface [17, 31, 71]. The sub-wavelength structures are designed to locally change the amplitude, polarization and phase of an incident beam so that various optical devices can be realized in a compact configuration [72, 73, 74, 61, 75, 76, 77, 78, 79, 80, 26, 81, 33]. This becomes important as the demand for portable and wearable devices increases. Here, metasurfaces enable flat optics with new opportunities especially for compact camera modules [48, 18, 82, 22, 83, 84]. Recently, a near diffraction-limited meta-lens doublet in the near-infrared has been demonstrated [55]. To achieve better spatial resolution and for more possible applications, we present, in the visible, a meta-lens doublet showing diffraction-limited focusing along the focal plane for an incidence angle up to 25°. The design builds up on our previous works and corrects for the first time Petzval field curvature, coma aberration and other monochromatic aberrations in the visible [35, 47]. The meta-lens doublet presented in this chapter is based on the principle of the Chevalier Landscape lens [66]. It was the first widely used camera lens introduced after the invention of the photographic process based on film. Both, the Chevalier Landscape lens and our meta-lens doublet, have in common a smaller aperture in front of a focusing lens [85]. In the Landscape lens, the rays in normal and oblique incidence are separated by the small aperture and then focused by different parts of the lens so that one can tailor its curvature to reduce

aberrations, especially coma aberrations. In our case, the role of the aperture is replaced by an aperture with a metasurface (refer to aperture meta-lens hereafter).

3.3 Realization of the meta-lens doublet

Figure 3.1a shows a schematic of our meta-lens doublet. An incident beam passes through the aperture meta-lens and substrate before being focused by the focusing meta-lens. The meta-lenses are comprised of titanium dioxide (TiO2) nano-fins with the same length, width, and height but different rotations arranged on a hexagonal lattice (Fig. 3.1b) [33]. Figure 3.1c-d shows the dimensions of each nano-fin. A phase profile (x,y) is imparted through the rotations of nano-fins based on the principles of Berry phase [19, 20]. Each nanofin is designed as a half-wave phase shifter converting the incident circularly polarized light into its orthogonal polarization state. The relations between $\varphi(x,y)$ and rotation angles $\alpha(x,y)$ follows: $\varphi(x,y) = 2\alpha(x,y)$, for the case of left-handed circularly polarized (LCP) light (Fig. 3.1e). The phase of the aperture meta-lens was chosen as follows:

$$\varphi_{AL}(x,y) = \sum_{n=1}^{5} a_n \left(\frac{\rho}{R_{AL}}\right)^{2n} \tag{3.1}$$

and similarly, for the focusing meta-lens:

$$\varphi_{FL}(x,y) = \frac{2\pi}{\lambda_d}\left(\sqrt{x^2+y^2+f^2} - f\right) + \sum_{n=1}^{5} b_n \left(\frac{\rho}{R_{FL}}\right)^{2n} \tag{3.2}$$

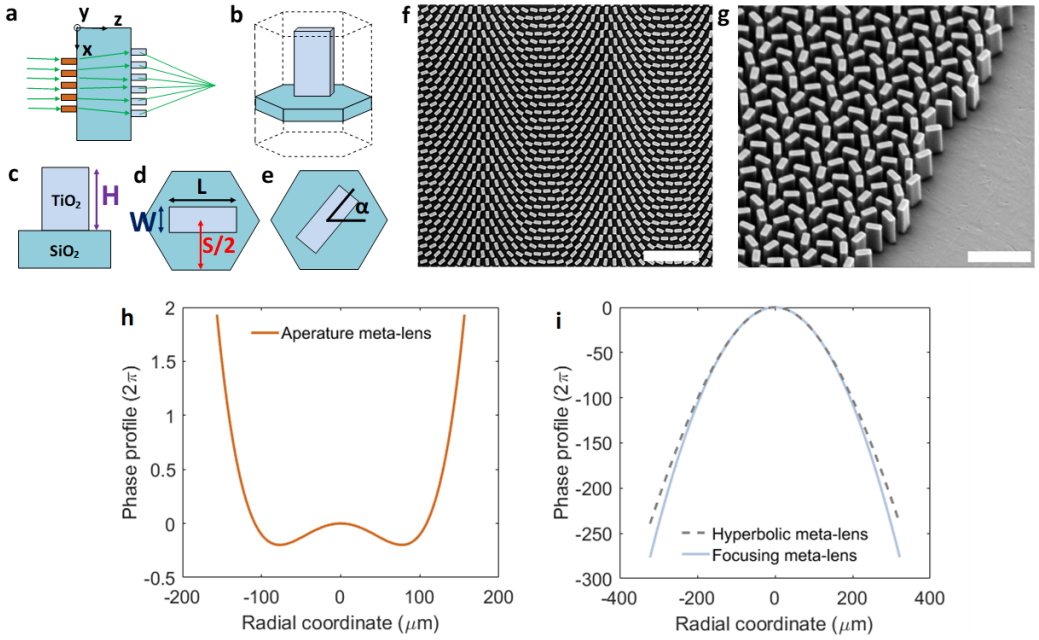

Figure 3.1: Design, phase profiles and the scanning electron microscope images of meta-lens doublet. (a) A schematic of the meta-lens doublet. The meta-lens doublet comprises two meta-lenses: aperture meta-lens (depicted in orange) and focusing meta-lens (depicted in light blue) patterned on both sides of a 0.5-mm-thick glass substrate, each meta-lens consists of an array of nano-fins with different rotation angles. (b-e) Geometric parameters of the nano-fin. The nano-fins are arranged in a hexagonal unit cell. (c-e) Side and top views of the hexagonal unit cell. The nano-fin dimensions are W = 95, L = 250, H = 600 and S = 320nm. (f) Top-side view SEM micrograph of the focusing meta-lens. Scale bar: 2000nm. (g) Side-view SEM micrograph at the edge of the focusing meta-lens. Scale bar: 1000nm. (h) Phase profile of the aperture meta-lens to correct positive and negative spherical aberrations. (i) A comparison for the phase profile of focusing meta-lens and hyperbolic meta-lens.

Here, λ_d is the design wavelength (= 532nm), f is the focal length (=342.3 µm, $\rho = \sqrt{x^2+y^2}$ is the radial coordinate, x and y are position coordinates of each nano-fin with respect to an origin at the center of each lens, R_{AL} and R_{FL} are the radii of the aperture and focusing meta-lens, respectively. In Eq. (3.2) we added a polynomial onto the hyperbolic phase profile to correct aberrations. The coefficients a_n and b_n are optimization parameters in our ray-tracing algorithm. They were determined such that all rays for various incidence angles up to 25° falls within diffraction-limited Airy disks (see Tab. 3.1 and 3.2 for the coefficients) [56].

$R_{\mathrm{AL}}(\mu$ m)	a_1	a_2	a_3	a_4	a_5
156.41968	-13.5078	22.5578	-5.3161	6.8526	-2.1028

Table 3.1: Phase profile of the aperture meta-lens

$R_{\mathrm{FL}}(\mu$ m)	b_1	b_2	b_3	b_4	b_5
321.4889	4.9531	-15.8389	2.9388	-0.0589	-0.00167

Table 3.2: Phase profile of the focusing meta-lens

Both aperture meta-lens and focusing meta-lens were fabricated by electron beam lithography followed by atomic layer deposition [28]. They were aligned through alignment marks patterned on both sides of a substrate. Figure 3.1f and 3.1g show electron microscope images for the focusing meta-lens, respectively. The phase profile of Eq. (3.1) and Eq. (3.2) were imparted assuming incident LCP and RCP light for the aperture and focusing meta-lens, respectively. The first term of Eq. (3.2) shows a hyperbolic shape, and we refer to a meta-lens with this phase profile as hyperbolic meta-lens hereinafter. Figure 3.1h-i show the phase plots

based on Eq. (3.1) and Eq. (3.2) for the aperture meta-lens and focusing meta-lens, respectively. We found that the aperture meta-lens has a phase profile similar to a Schmidt plate, which is widely used to correct spherical aberration [86, 87]. This phase profile results in converging chief rays and diverging marginal rays. The phase profile of the focusing meta-lens has a stronger phase gradient at the edge than that of the hyperbolic meta-lens (dashed gray line in Fig. 3.1i, plotted with the first term of Eq. (3.2) only).

3.4 Ray reasoning of the doublet

Figure 3.2a shows the ray diagram for the hyperbolic meta-lens, which is only capable of achieving diffraction-limited focusing at normal incidence. The inset shows a magnified plot of the rays near the focal plane. At oblique incidences, it suffers strong aberrations; we found that this cannot be corrected by adding another metasurface as a correcting lens without modifying its hyperbolic phase profile, because the ray diagrams for different angles of incidence are significantly different, as shown in the inset of Fig. 3.2a. Figure 3.2b shows the case for the focusing meta-lens without the aperture meta-lens. The focusing meta-lens has the same design parameter as the meta-lens doublet. Through the stronger phase gradient at the edge (see light blue curve in Fig. 3.1i) than that of the hyperbolic meta-lens, the marginal rays get bent more towards the optical axis (focusing before the focal plane); while chief rays get bent less (focusing behind the focal plane). These effects are known as positive and negative spherical aberra-

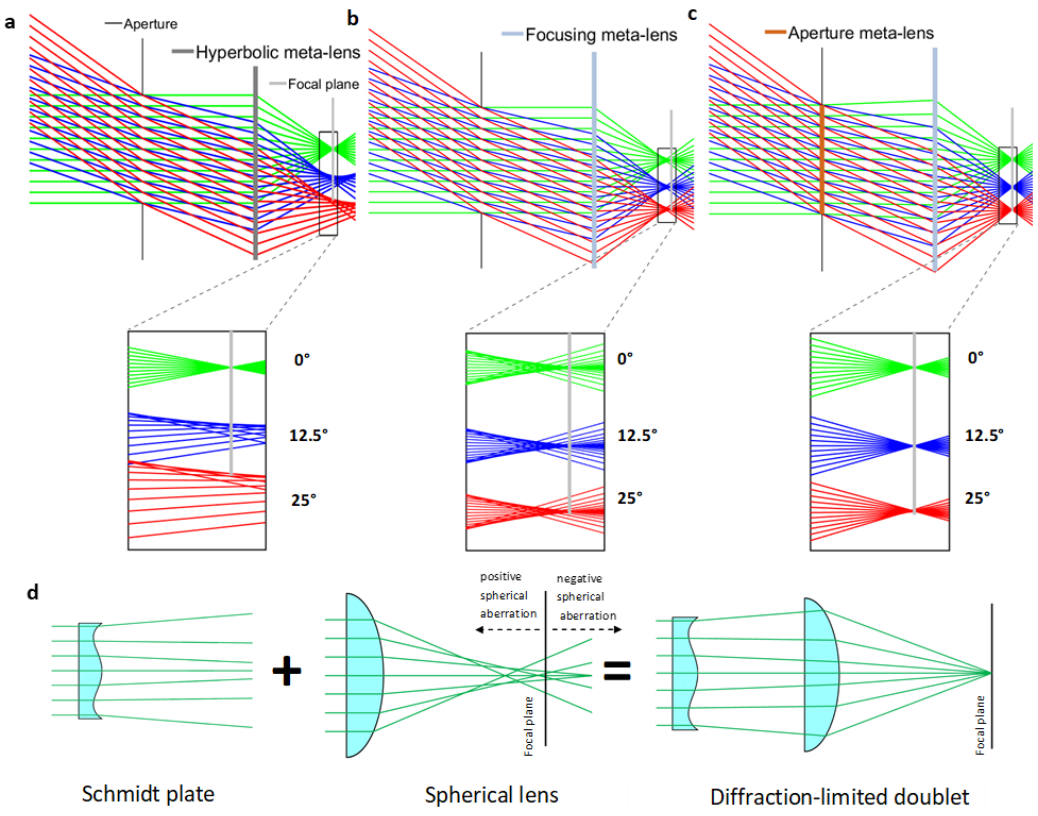

Figure 3.2: Ray diagrams for explaining the principle of correcting aberrations. (a) Ray-diagram of a meta-lens with hyperbolic phase profile showing large aberrations at oblique incidence. (b) Ray-diagram of the focusing meta-lens with phase profile shown in the light blue curve in Fig. 3.1i. (c) Ray diagram obtained by adding the aperture meta-lens resulting in diffraction-limited focusing along the focal plane. The insets of (ac) show the magnified plots near their focal planes. (d) The operation of the meta-lens doublet in terms of the correction of spherical aberration is analogous to that of a Schmidt plate combined with a spherical lens. The positive and negative spherical aberrated marginal and chief rays are corrected through the concave and convex curvature of the Schmidt plate.

tion, respectively. The phase profile of the focusing meta-lens results in similar ray diagrams (Fig. 3.2b) for different incidence angles, and therefore provides a possibility to correct the aberrations. In Fig. 3.2c, with the aperture meta-lens, the positive and negative spherical aberrations are corrected to realize diffraction-limited focusing along the focal plane. Figure 3.2d shows an analog ray diagram with refractory lenses. Spherical aberrations are corrected by the Schmidt plate in such a way that marginal rays are diverged, which increases the effective focal length while chief rays are converged, which decreases the effective focal length.

3.5 Focal spot measurements

Figure 3.3a shows a schematic setup for measuring the size of the focal spot for different angles of incidence. An objective of NA = 0.95 with a tube lens (f = 180 mm) is used to magnify the focal spot by 100 times on a camera with a pixel size of 180 µm. The sample, objective, tube lens and camera are mounted on a rail to adjust the angle of incidence. The light source is a λ = 532nm laser with a bandwidth of 30 GHz (28 pm), which means that chromatic aberrations can be neglected. Figure 3.3b-f show the focal spots for an incidence angle up to 25°. Slightly deformed focal spots result from the misalignment of aperture and focusing meta-lens (Fig. 3.4). Figure 3.3g shows the full-widths at half maximum (FWHMs) $\frac{\lambda_d}{2\mathrm{NA}}$ for all incidence angles up to 25°. Their Strehl ratios are approximately equal to or larger than 0.8 (Fig. 3.5), which meets the requirement of diffraction-limited focusing [88]. Slight deviations arise from small misalignments between the two

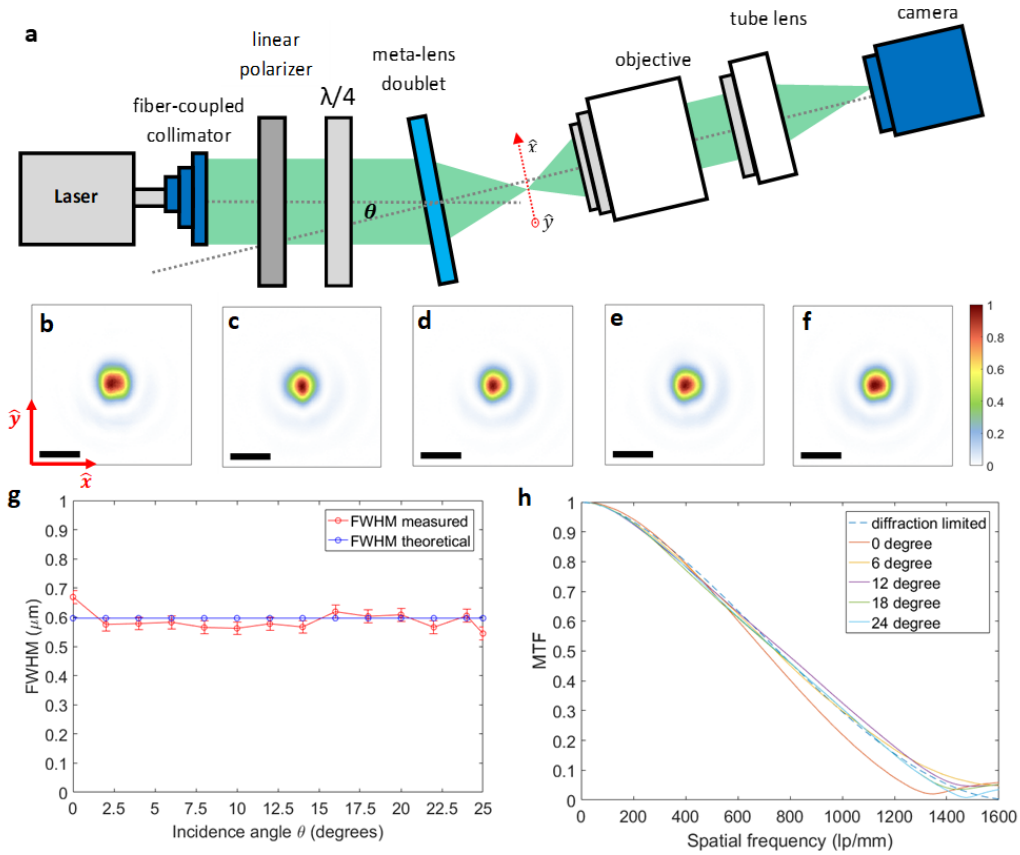

Figure 3.3: Focal spot characterization for different angles of incidence () at λ_d= 532nm. (a) Focal spot measurement setup. (b-f) Focal spot intensity profile at (b) 0°, (c) 6°, (d) 12°, (e) 18°, (f) 25° incidence angle θ. Scale bar: 1.1 μm. Their FWHMs along the $\vec{x}$ direction are shown in (g) in comparison to modeling. (h) Measured Modulation Transfer Function (MTF) curve along $\vec{x}$ direction at different incidence angles. Horizontal axis is in units of line pair per mm. A diffraction-limit MTF curve (blue dashed line) is provided as reference.

meta-lenses and finite camera pixel size. Figure 3.3h shows the diffraction-limited modulation transfer function MTF for different incidence angles. Simulated focal spots with incidence angles beyond 25° are provided in Fig. 3.6 for reference. We obtained the MTF by taking the modulus of the discrete Fourier transformation of the intensity distribution at the intersection between the focal plane and the plane of incidence ($\vec{x}$ direction in Fig. 3.3a). In general, the MTF value drops for large spatial frequencies with a cut-off frequency of $\frac{2\mathrm{NA}}{\lambda_d}$. The resolution limit of an imaging system is defined by the inverse of the spatial frequency at which the MTF has a value of 0.1.

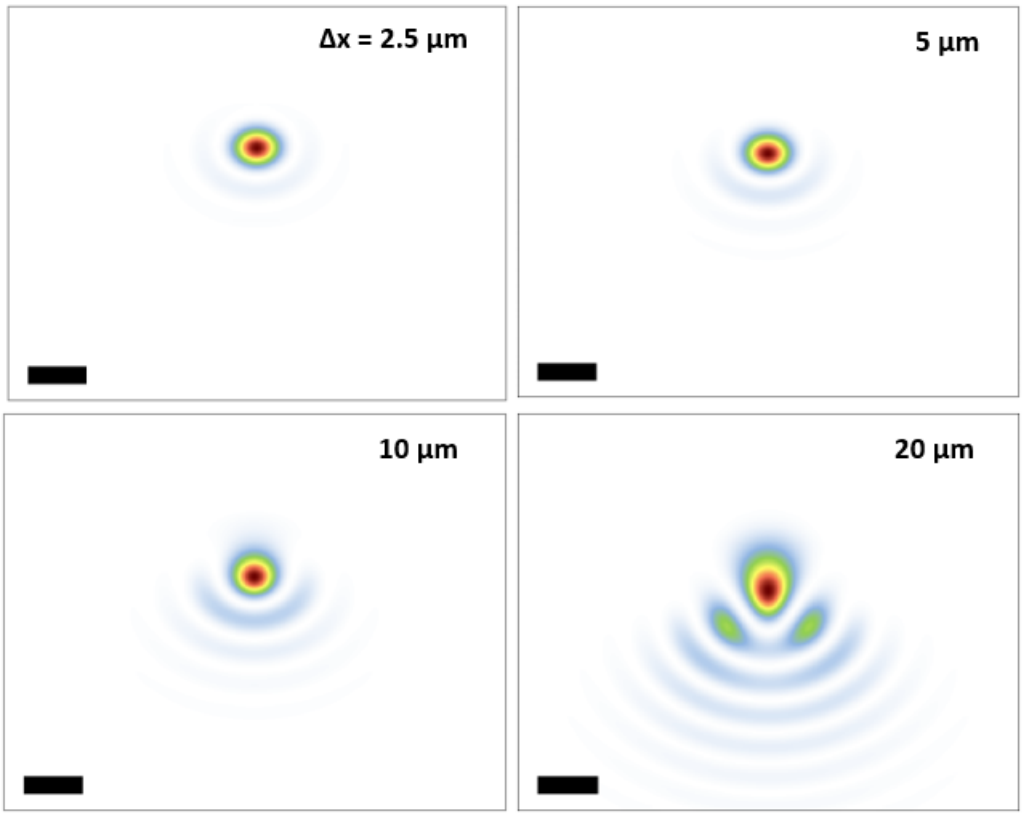

Figure 3.4: Analysis of the effect of fabrication misalignment between aperture and focusing meta-lens. Simulated focal spot for 2.5 µm, 5 µm, 10 µm and 20 µm fabrication misalignment between the aperture and focusing meta-lens along $\vec{x}$ direction as shown in Fig 3.1a in case of normal incidence. Red corresponds to high intensity. Blue corresponds to low intensity. Scale bar: 1.1 µm.

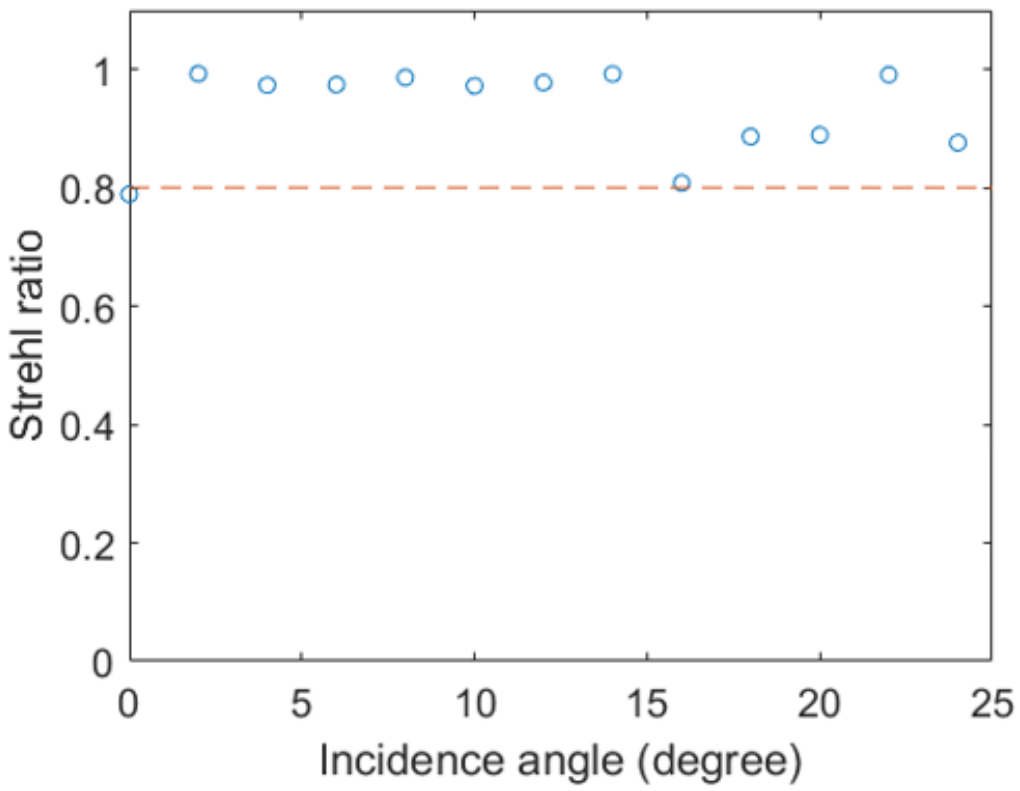

Figure 3.5: A Strehl ratio larger than the dashed line corresponds to a diffraction-limited imaging system.

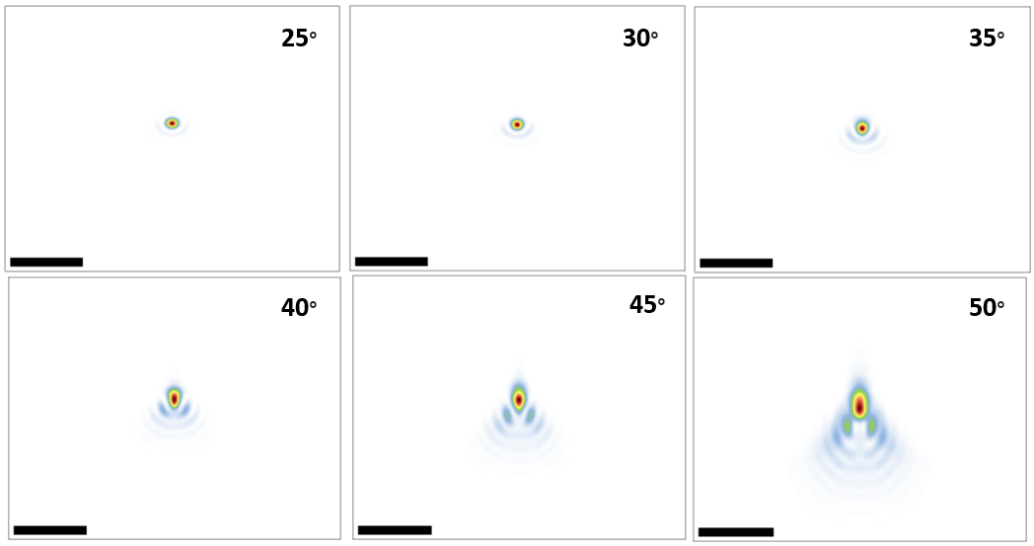

Figure 3.6: Simulated focal spot intensity when the incidence angle is larger than 25. Red corresponds to high intensity. Blue corresponds to low intensity. Scale bar: 5 µm.

3.6 Widefield imaging

Subsequently, we used this meta-lens for widefield imaging. Figure 3.7 shows the schematic setup for imaging the 1951 US Air Force resolution target. The target is placed at the focal plane and then imaged through the meta-lens doublet (Fig. 3.7a). To reduce laser speckle, a supercontinuum laser (SuperK, NKT Inc.) with 5nm bandwidth is used. The resolution target consists of stripe groups: each group contains three vertical and horizontal bars with an equal line width and gap. Here we image the group with a line width of $\approx 2.2\,\mu$m. From Fig. 3.7b to 3.7h, we move our meta-lens doublet in steps of $25.4\,\mu$m away from the optical axis to characterize image quality; this corresponds to different fields of view of the meta-lens doublet. The largest movement $\approx 152\,\mu$m (Fig. 3.7h) corresponds to a diffraction angle equal to 25°; the horizontal bars become blurred because chromatic aberration becomes more significant at larger angles (Fig. 3.8 and 3.9).

The measurement setup includes a super continuum laser (NKT "SuperK") equipped with an acousto-optic tunable filters (NKT "Select") with a fiber output. A narrowband green laser (Laserquantum, Ventus532) with a bandwidth of 30 GHz 28 pm was selectively used. The incident beam was collimated by a fiber collimator (RC12APC-P01, Thorlabs) and then circularly polarized through a wire grid polarizer (Thorlabs WP25L-UB) followed by a quarter wave plate (Thorlabs AQWP05M-600).The focal size is magnified by an objective (Olympus, MPLAPOn, 100x, NA = 0.95) paired with a tube lens (Thorlabs, AC508-180-A-ML), then imaged on a monochromatic camera (Edmund Optics, EO-5012).

Images of the resolution target were taken with a Thorlabs DCC1545M camera.

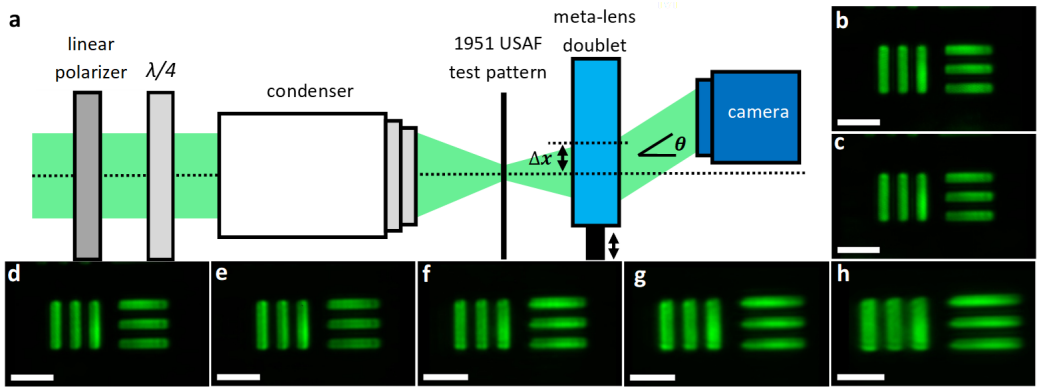

Figure 3.7: Imaging with the meta-lens doublet for the element 6 in group 7 of 1951 US air force resolution target: 2.2 µm line width and gap. (a) Imaging set-up using meta-lens doublet. The illumination light source is from a laser centered at 532nm with a bandwidth of 5nm. (b-h) Images taken by moving the meta-lens doublet 25.4 µm per step with respect to the center of the target. Each movement, Δx, corresponds to an angle θ. Scale bar: 11 µm. The (Δx,θ) from (b) to (h) are (0 µm, 0°), (25.4 µm, 4.11°), (50.8 µm, 8.26°), (76.2 µm, 12.48°), (101.6 µm, 16.83°), (127.0 µm, 21.33°), and (152.4 µm, 26.05°)

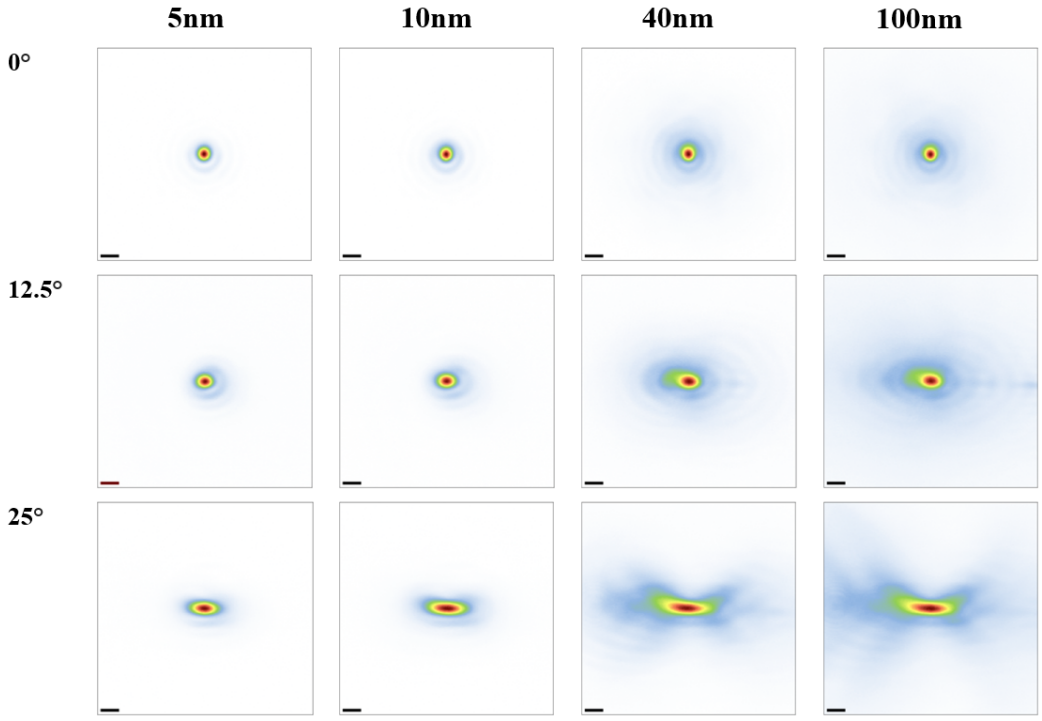

Figure 3.8: Measured focal spot intensities for different bandwidths (depicted on the top) at different angles (degrees) of incidence using a laser with center wavelength at 532nm. Scale bar: 1.1 µm.

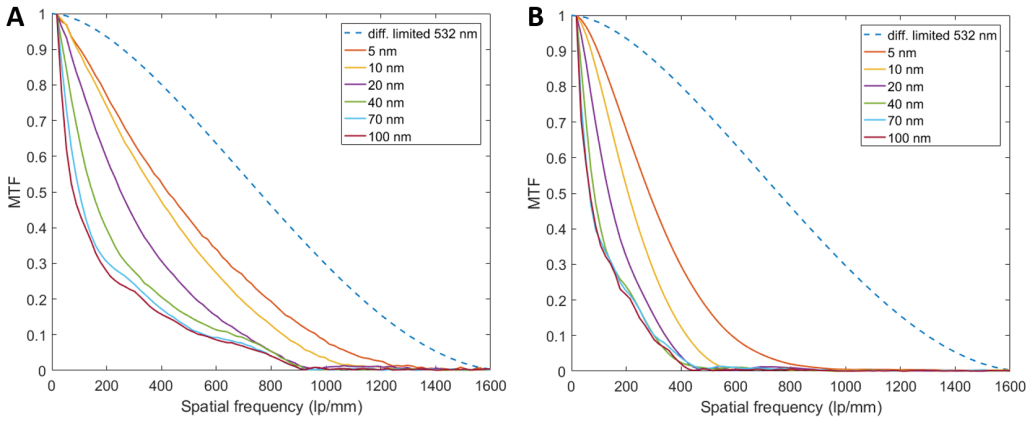

Figure 3.9: Measured modulation transfer function for various angles of incidence at (A) 12.5 degree, (B) 25 degree. The light source is from a laser with a center wavelength of 532nm and various bandwidths labeled in the legend.

3.7 Chromatic properites of the meta-lens doublet

Figure 3.10a-j show the images when we place the target at the center of the meta-lens doublet in normal incidence. Figure 3.10a-f show the images taken using a tunable laser as light source with a center wavelength at 532nm of various bandwidths from 5nm to 100nm, while Fig. 3.10g-j show that of difference center wavelengths with a constant 5nm bandwidth. In Fig. 3.10f, although the feature can still be resolved, the contrast drops significantly when the laser bandwidth increase to 100nm. This represents a drop in the MTF value as shown in Fig. 3.10k, which results from chromatic aberration: focal length changes as wavelengths (Fig. 3.10l). The chromatic aberration can be reduced by several approaches: refractive/diffractive compound lens [37], dispersion engineering of nanostructure resonances [39, 38] or designing a nanostructure that can provide more than 2 phase modulation [89, 40, 90]. Even though the meta-lens doublet is designed at 532nm, it is still capable of resolving the target clearly at other wavelengths with 5nm bandwidth. Figure 3.10m) shows the MTF curve as a quantitative analysis of Fig. 3.10g to 3.10j. Also notable, the meta-lens doublet has low temperature dependence from 25°C to 70°C. Its focal spot remains diffraction-limited (Fig. 3.11). The maximum focusing efficiency of the meta-lens doublet is about 50% (Fig. 3.12).

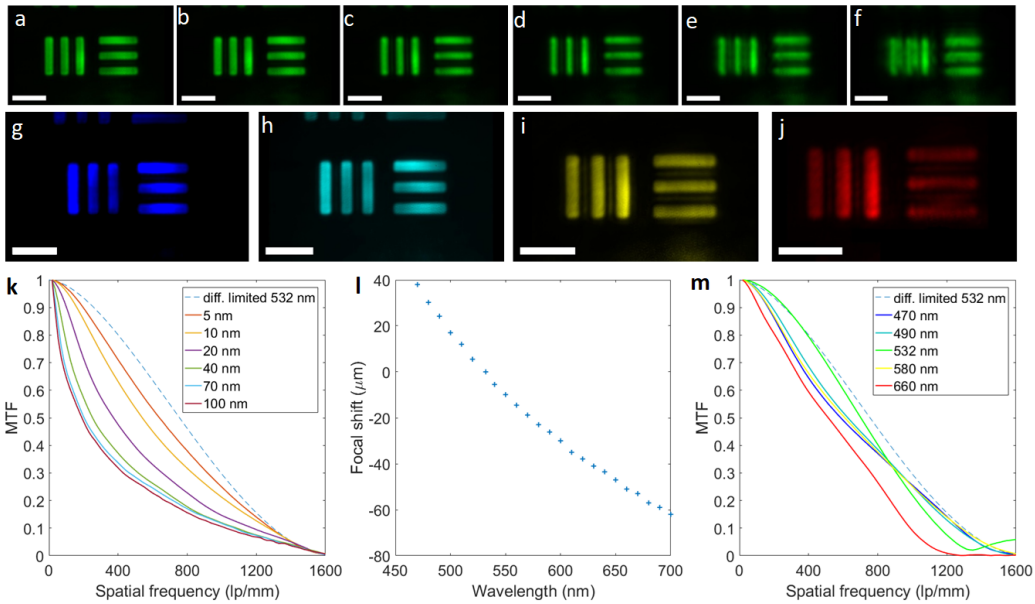

Figure 3.10: Analysis of the chromatic properties of the meta-lens doublet.(a-f) On-axis imaging at normal incidence with laser center wavelength λ= 532nm and a bandwidth of (a) 5nm, (b) 10nm, (c) 20nm, (d) 40nm, (e) 70nm, (f) 100nm. Scale bar: 11 µm. (g-j) On-axis imaging with a laser bandwidth of 5nm and a center wavelength at (g) 470nm, (h) 490nm, (i) 580nm and (j) 660nm. Scale bar: 11 µm. (k) MTF for different bandwidths at 532nm in normal incidence. (l) Chromatic focal length shift of the meta-lens doublet as a function of wavelength. Reference is the designed wavelength λ_d= 532nm. (m) MTF for different laser center wavelengths with a 5nm bandwidth.

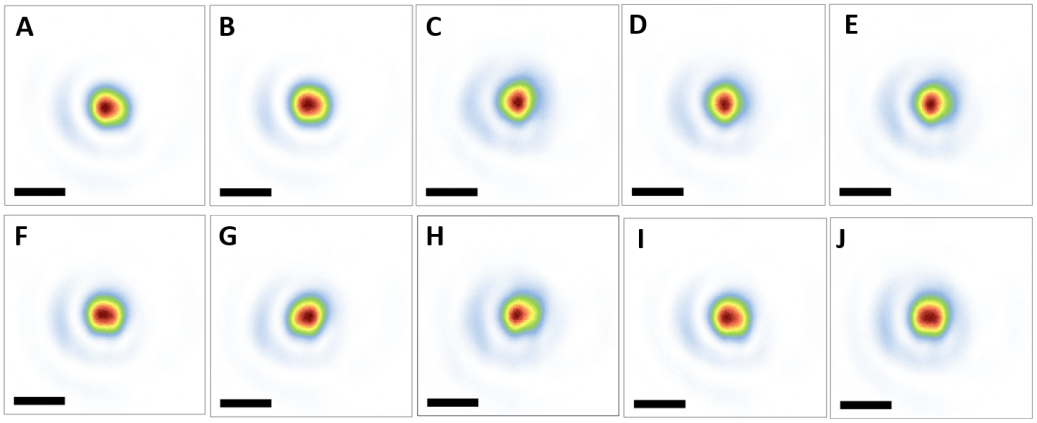

Figure 3.11: Measured focal spot intensity when heating the meta-lens to different temperatures. The incident light is from a 532 nm laser with a bandwidth at 30 GHz (28 pm) at normal incidence. Temperatures: (A) 25°C, (B) 30°C, (C) 35°C, (D) 40°C, (E) 45°C, (F) 50°C, (G) 55°C, (H) 60°C, (I) 65°C and (J) 70°C. Scale bar: 1.1 µm.

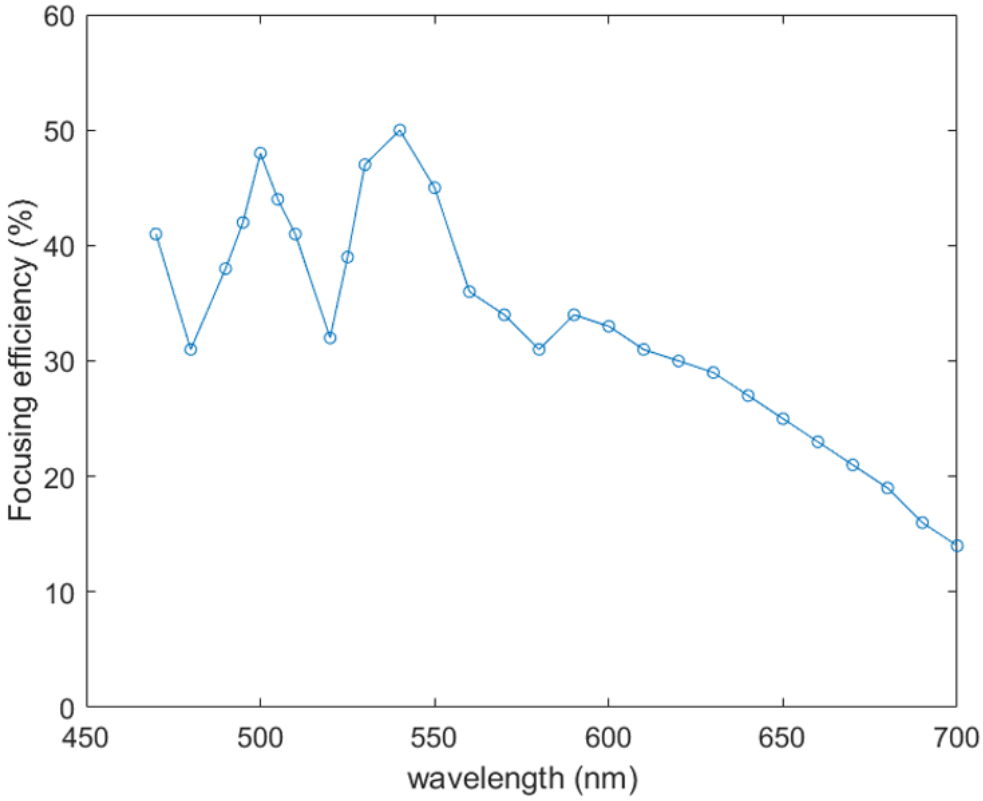

Figure 3.12: Focusing efficiency as a function of wavelength. The focusing efficiency is defined as the power of the focal spot divided by the incident light in the case of circularly polarized light. The two peaks can result from the variations in length, width and height of the nano-fins between aperture and focusing meta-lenses, since they were manufactured separately.

3.8 Fabrication of the visible meta-lens doublet

3.8.1 Fabrication of alignment marker

Electron beam lithography (EBL) alignment markers are fabricated on both side of the substrate with photolithography using a two layer lift-off process. First the substrate (fused silica) is cleaned via ozone stripper for 5 minutes, Piranha etch for 15 minutes, and acetone and isopropyl alcohol (IPA) sonication bath for 3 minutes each. The Piranha etch is used consistently through the whole fabrication process with a 3:1 mixture of concentrated sulfuric acid (H2SO4) with hydrogen peroxide (H2O2). The first layer of the lift-off process is a photo-insensitive resist, LOR3A (MicroChem), spin coated with 3000 rotations per minute (RPM), baked at 180 °C for 7 minutes. The second layer is a photosensitive Shipley resist, S1805, spin coated with 3000 RPM, baked at 115 °C for 3 minutes. The sample is exposed with dose of $60\,\mathrm{mJ/cm^2}$ in the Heidelberg MLA150 tool. For development MF-319 is used for 30 seconds. Chromium is thermally evaporated before the resist is removed with a 24 hour bath of PG-Remover. After an acetone sonication bath for 3 minutes the steps between ozone stripper and PG-Remover are repeated for the backside of the substrate. Large photolithgraphy alignment marks are used to align the back side to the front side of the substrate using the SUSS MA6 Mask Aligner tool.

3.8.2 TiO2 metasurface fabrication

To clean the substrate from any possible remaining residue from the photolithography process, the substrate is again cleaned via ozone stripper, Piranha etch, acetone and isopropyl alcohol (IPA) sonication. Electron sensitive resist ZEP520A is spin coated with 1750 RPM, baked at 180 °C for 5 minutes. ESpacer 300Z is spin coated at 1750 RPM on the resist to avoid charging effects because of the poor conductivity of the fused silica substrate. Then EBL is carried out by Elionix ELS-F125 at 125 kV. The aperture meta-lens is written first. Deionized water is used to remove the ESpacer. Cooled to 5 °C, O'Xylene is used for 1 minute to develop the sample. During development the sample is moved back and forth in the bath to increase surface interaction. After an isopropyl alcohol (IPA) dip, TIO2 is deposited with atomic layer deposition (ALD) in the Savannah Cambridge Nanotechnology tool. The backside is protected with scotch tape. Next, TIO2 is top-down etched through inductively coupled plasma etch (ICP-RIE) with Uniaxial Shuttleline ICP RIE tool. The remaining resist is lifted off with a 24 hour PG-Remover bath. Before the fabrication of the focusing meta-lens the extensive cleaning procedure of ozone stripper, piranha etch, acetone bath and IPA bath is carried out again. No sonication is used to avoid damaging the aperture metasurface. Five layers of polymethyl methacrylate (PMMA) each spin coated at 1000 RPM, baked at 180 °C for 90 seconds are used as protective material for the aperture metasurface. Next, ZEP520A (Zeon Chemicals) is spin coated on the backside of the substrate at 1750 RPM, then extensively baked for 30 minutes at 150 °C, as PMMA has a melting point of 160 °C. After EBL for the focusing

meta-lens, development, ALD and etching steps were repeated as before. This time no scotch tape is needed during the ALD process due to PMMA. PMMA is removed with ZEP520A during a 24 hour PG-Remover lift-off bath. During the bath the sample is held straight to avoid contact of the metasurfaces with the beaker. As a final step to remove any possible residue the sample is held with a pair of tweezers in a Piranha solution for 5 minutes.

3.9 Conclusion

We have demonstrated a meta-lens doublet consisting of nano-structures at wavelength λ_d = 532nm, with a numerical aperture of 0.44, a focal length of 342.3 µm and 50° field of view. The meta-lens doublet is capable not only of performing diffraction-limited focusing, but also of realizing high quality imaging along the focal plane. Unlike in traditional Fresnel lenses, the use of nano-structures can provide another degree of freedom to engineer the chromatic aberration. In addition meta-lens doublets can be mass produced by deep ultraviolet lithography or nano-imprinting. The meta-lens doublet can find many applications in laser-based microscopy and spectroscopy as well as in computer vision and machine vision.

Chapter 4

Sequentially stacked microfluidic droplet maker

4.1 Summary

We have demonstrated a sequentially stacked microfluidic droplet maker. Hydrophobic and hydrophilic surfaces are produced on independent layers enabling a scalable surface treatment batch process prior to assembly. Since each part can be mass-produced, the sequentially stacked microfluidic droplet maker uniquely combines scalability in surface treatment with scalability in component manufacturing.

4.2 Introduction

Microencapsulation has long been used as a mean for protection and/or controlled release of active ingredients in food, pharmaceuticals, agrochemicals, cosmetics, nutraceuticals and materials [91, 92, 93]. The applications range from taste masking in food to extending efficacy of drugs. In its most common form the active ingredients are encapsulated within solid microbeads, e.g. through spray drying [92]. However, longer shelf-life times and higher loading percentages are achieved through a spatial separation of cargo and carrier in a spherical core-shell structure [92, 94, 95]. As those microcapsules are more desirable, because of their properties, they are also more difficult to make [92, 96, 97].

Monodisperse spherical core-shell emulsions of emulsions can be produced through microfluidics, which are known as double emulsions [98, 99]. The shell of double emulsions can be solidified to obtain microcapsules [93, 100]. The microfluidic encapsulation process is mild without large shear forces and therefore an ideal candidate for sensitive therapeutic cargo such as macrobiotic cells, enzymes and monoclonal antibodies which do not survive the harsh conditions of traditional microencapsulation methods [101, 102]. While the high throughput production of microbeads with microfluidics is straight forward [103], the high throughput production of microcapsules has only been realized through the re-encapsulation of the microbeads [104, 105] or through the omittance of surface treatment [106], both results in less stable operation. An industrial-scale microfluidic droplet maker (MDM) making microcapsules at a single junction of inner, middle and outer phase is an unmet challenge.

In this chapter, we propose a sequential stacked microfluidic droplet maker (SSMDM), depict in Fig. 4.1(a). In the droplet generation region, the fluid flow in SSMDM is orthogonal to each substrate layer of the device and hence the hydrophobic and hydrophilic surfaces are spatially separable, which allows surface treatment in batch processes. Each layer remains highly scalable through the same manufacturing processes mentioned above [104, 106, 107, 108, 109, 110, 111], therefore the SSMDM uniquely combines scalability in surface treatment with scalability in component manufacturing (Fig. 4.1(b)).

Todays MDMs can be characterized as glass capillary MDMs [99] or in-plane MDMs [104, 105, 106, 111]. In an in-plane MDM the channels are on a single

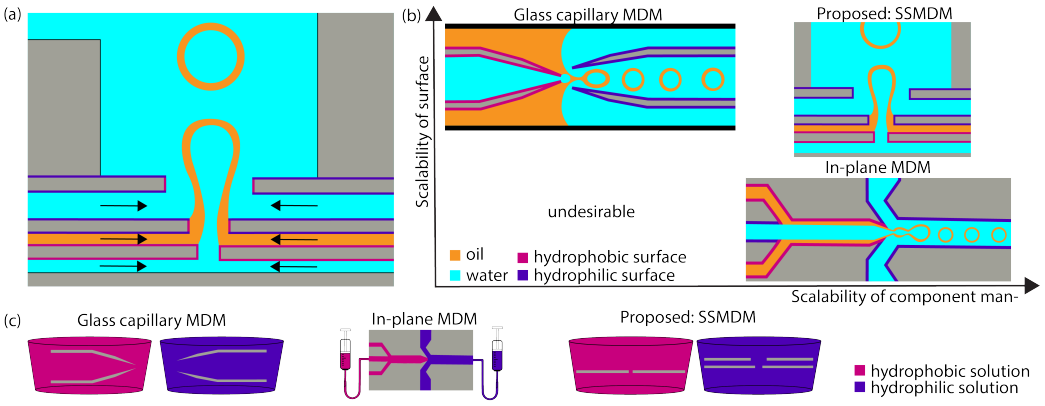

Figure 4.1: Scalability of the sequentially stacked microfluidic droplet maker (SSMDM). (a) SSMDM comprised of multiple stacked layers. Channel and pore layers are alternately stacked. The size of the inner, middle and outer pore is 100 µm, 360 µm and 600 µm respectively. (b) Unlike previous methods, SSMDMs combine scalability of surface treatment with scalability of component manufacturing. (c) Surface treatment method for a glass capillary microfluidic droplet maker (MDM), an in-plane MDM, and a SSMDM. The layers of the SSMDM can be put in hydrophobic or hydrophilic solutions. A careful alignment of those solutions inside the droplet maker is not required.

substrate. The fluid flows parallel to the main surface of the substrate. Since the hydrophobic and hydrophilic surfaces are attached to the same substrate, it prevents any batch surface treatment process. As shown in Fig. 4.1(c), a careful fluid alignment of hydrophobic and hydrophilic solutions inside the device is required. However, the channels and pores of in-plane MDMs can be produced through various highly scalable manufacturing processes such as laser cutting [110], hot embossing [107, 108, 109], stamping [107], glass etching [104] or soft-lithography [106, 111]. On the contrary, the nozzles of glass capillary MDMs are difficult to make since the glass needs to be precision ground to the right size. But glass capillary MDMs can be surface treated in a batch process prior to assembly. For the SSMDM, we drew our inspiration from the Gutenberg printing press and modern integrated circuits. Here, the sequential addition of 2D patterned materials has been transformative enabling book printing and modern computers.

4.3 Experimental realization

Figure 4.2(a) shows the geometry of our prototype. From the SSMDM inlets the fluid flows through narrow, serpentine channel towards the droplet generation region. The high resistance of the serpentine channels reduces any fluctuations from the pumps. Each phase is delivered from both sides, so that the double emulsions are balanced in the center of the droplet generation region. The inner and middle phase channels are perpendicular, which provides a stabilizing pressure from each side. The size of the inner, middle and outer pore is 100 µm, 360 µm and 600 µm

respectively (Fig. 1(a)). We have experimentally varied the size of the middle pore and found the device is not stable, producing single emulsions, when the middle pore size is close to the inner or outer pore size.

Figure 4.2(b) shows a photograph of the SSMDM. Our SSMDM prototype is made of (hydrophobic) PET layers and double-sided adhesive layers (both 125 µm thick) which are stacked alternatively. When the surface needs to be hydrophilic, we used a commercially available, hydrophilic treated polyester film (125 µm thick). The channels were laser cut and the pores micro-drilled. Since the micro-drilling was post-surface treatment, this leaves the middle pore hydrophobic. Some surfaces do not have the right wettability, which could be solved by protecting one side of the layers with a spin-coated resist during the surface treatment process.

Figure 4.2(c) shows the SSMDM located below the manifold channels. Each channel branch for the inner, middle and outer phase of the manifold is large with equal length to maintain even pressure at SSMDM inlets. The size of the manifold channels makes the pressure differential through them negligible. The manifold channels have varying penetration depths, delivering the different phases into their assigned layers. The inner phase goes to the bottom layer, while the middle and outer phase go into the layers above.

The double emulsions exit the droplet generation region through the outlet channel on top. As the manufacturing process does not impose any constraints on the size of the outlet channel, the outlet channel can be designed large enough to avoid squeezing of the double emulsions. Balancing the forming double emul-

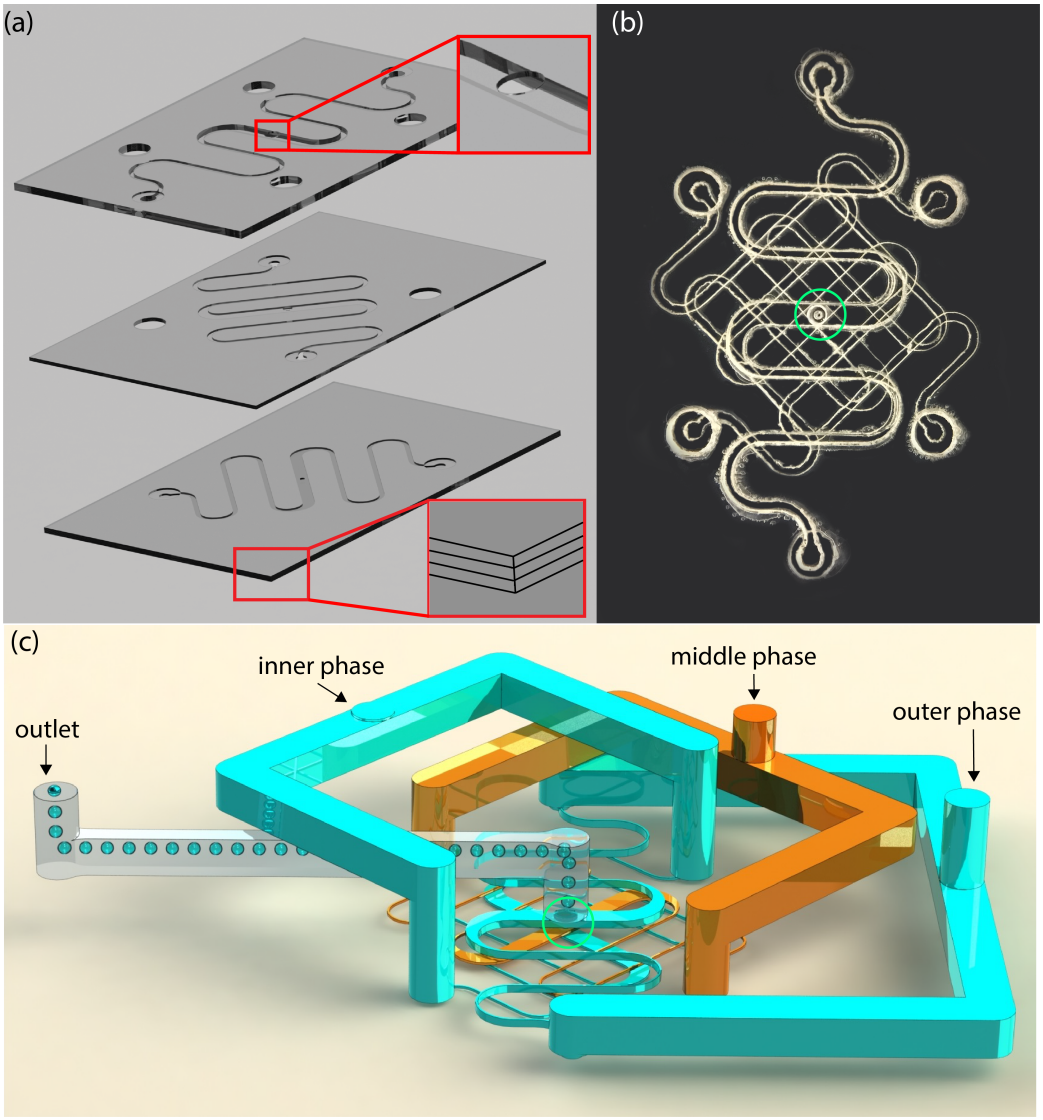

Figure 4.2: Realization of sequentially stacked microfluidic droplet maker (SSMDM). (a) 3D Side-view schematics of the SSMDM. (b) Top-view photograph of the SSMDM. The outlet is in the center. Each phase has two directly opposing inlets which are connected to the droplet generation region with narrow, serpentine channels. (c) SSMDM below the distribution channels for inner, middle and outer phase. To maintain even pressure at SSMDM inlets each distribution branch is large with equal length.

sions from all sides and the avoidance of squeezing through a large outlet channel cannot easily be achieved with in-plane MDMs [111], but the SSMDM enables it through the 3D geometry.

While the SSMDM is running, we observe the double emulsions in the outlet channel, Fig. 4.2(a). Figure 4.3(a) shows bright field image $I(x,y)$ of a double emulsion (w/o/w). An absorption dye is inside the inner phase to achieve higher contrast. Figure 4.3(b) shows the magnitude of the intensity gradient $|(\frac{dI(x,y)}{dx}, \frac{dI(x,y)}{dy})|$ of the bright field image. The center coordinates of the double emulsion were found with a Hough transform [112]. We averaged the pixels with the same radial distance to the center of the double emulsion and get the intensity as a function of radial distance. Afterwards we apply a 1D Gaussian filter to reduce the noise [113]. The intensity curve is shown in Figure 4.3(c).

Now, we can determine the inner (r_1) and outer radius (r_2) of the double emulsion through the local minima in the magnitude of the intensity gradient. We can see that the first minimum corresponds to a minimum in the intensity, which is the inner radius of the double emulsion. The second minimum corresponds to a maximum in the intensity which is the shell center. The third minimum corresponds to the outer radius of the double emulsion. The advantage of taking the gradient instead of the intensity is that this method is less sensitive to noise. However, for some images the noise would still be too great to accurately determine the inner and outer radius, so we wrote a GUI software that allows the user to decide whether a double emulsion should be accepted or rejected for the measurement.

Figure 4.3(d) shows a histogram of inner and outer radius of 450 different

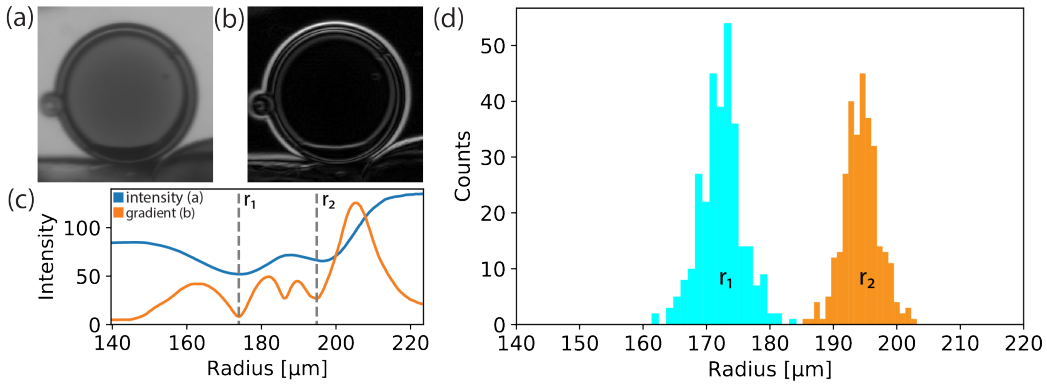

Figure 4.3: Droplet Analysis of sequentially stacked microfluidic droplet maker (SSMDM). (a) Bright field image I(x,y) of a droplet inside the outlet channel. (b) Magnitude of the intensity gradient $|(\frac{dI(x,y)}{dx}, \frac{dI(x,y)}{dy})|$ of the same bright field image. (c) Radially integrated intensity and gradient magnitude after filtering. The inner (r_1) and outer radius (r_2) of the droplet is determined through the local minima in the magnitude of the intensity gradient. (d) Histogram of r_1 and r_2 of 450 different droplets. $r_1 = 123.9\,\mu m \pm 2.42\,\mu m$. $r_2 = 139.19\,\mu m \pm 1.99\,\mu m$

double emulsions produced with a flow rate of 6, 3 and 50 ml/hr. for the inner, middle and outer phase respectively. The inner radius is 123.39 µm with a standard deviation of 2.42 µm, while the outer radius is 139.19 µm with a standard deviation 1.99 µm. This means 11.35% of the outer radius is the oil shell, which is close to the theoretical value of:

$$\frac{r_2 - r_1}{r_2} = 1 - \sqrt[3]{\frac{Q_1}{Q_1 + Q_2}} = 0.1264 = 12.64\% \tag{4.1}$$

given by Q_1, Q_2, the inner and middle phase flow rate respectively. The inner and outer phase is water with 3% PVA. The middle phase is mineral oil with 2% SPAN80.

4.4 Microfluidic manifold

High shell uniformity across different droplets can only be achieved when the flow rates of outer, middle and inner phase in each droplet maker is uniform as well. In this section, we study the flow uniformity in microfludic manifolds using a CFD finite element analysis.

First, we need to determine, how many devices, we need to multiplex. According to the U.S. Department of Agriculture, a typical spray drying facility has a daily production volume of 60 tons [114]. A microfluidic device producing 100 µm core-shell capsules has a typical production rate of 100 g per hour. To match the daily production rate of the spray drying facility 25,000 devices would need to be multiplexed. The fluid is divided into multiple channel branches. Each channel branch should have the same flow rate and velocity profile without turbulence.

Microfluidic channel can be model like electric resistors. The pressure ΔP is driving the fluid flow Q through a channel with resistor R.

$$\Delta P = RQ \tag{4.2}$$

As a first constraint to ensure that the flow rate is the same in each branch is that each path has the same length. This is best achieved with a tree structure like as shown in 4.4. The Reynolds number is a figure of merit of how turbulent fluid flow is. A high Reynolds number indicates turbulent flow. The Reynolds number

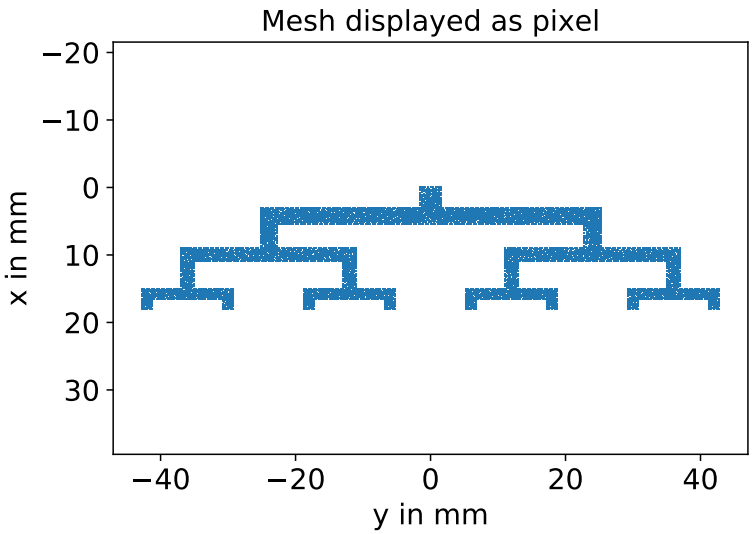

Figure 4.4: Tree branch manifold

is given by:

$$Re = \frac{\rho \overline{u} h}{\mu} \tag{4.3}$$

Here, ρ is the mass density of water, $\overline{u}$ is the mean velocity, μ the dynamic viscosity of water, and h is the width of the channel. We can calculate the mean velocity by integrating the plane Hagen-Poiseuille flow from Navier stokes equation $u(y) = \frac{G}{2\mu} y(h-y)$ with the pressure gradient G applied in the direction of flow:

$$\overline{u} = \frac{1}{h}\int_0^h u(y)dy = \frac{G}{2h\mu}\int_0^h y(h-y)dy = \frac{Gh^2}{12\mu} \tag{4.4}$$

The mean velocity is $\overline{u} = \frac{Gh^2}{12\mu}$. In order to have 25,000 devices running in parallel, 15 layers need to be stacked above each other. The final flow rate should be 10 mL/hr. The inlet size should be 3.2 cm. Assuming the channel width in each layer decreases by 20 percent, the final channel width would be 1 mm. We can

calculate the Reynolds number at each layer, the result is shown below.

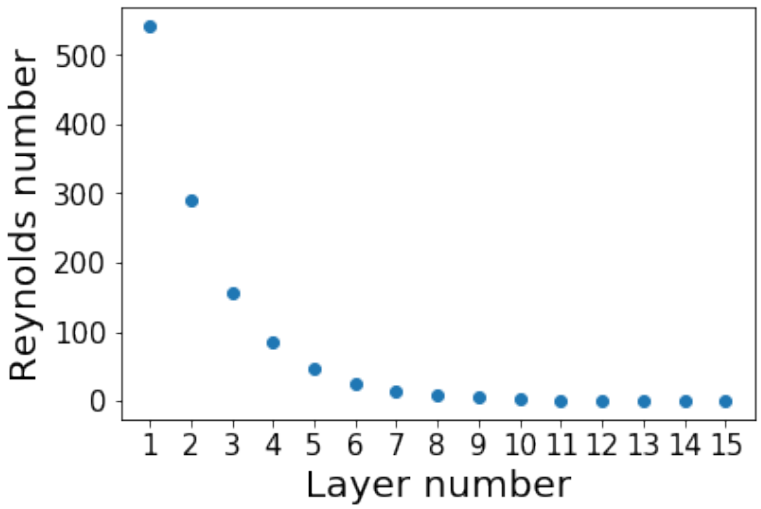

Figure 4.5: Layer 1 is the top most layer with the inlet size of 3.2 cm, each layer gets successively 20 percent smaller.

The picture below shows the velocity magnitude inside the manifold. We can see that the velocity stream lines are not always centered in the channel as the analytic solution of Navier Stokes equation would predict. Instead the fluid bounces inside the channel due to the junctions.

We can see that the flow rate varies greatly. The flow rate was obtained with Scipy's composite Simpsons rule method by integrating the velocity along the width of the outlet channel.

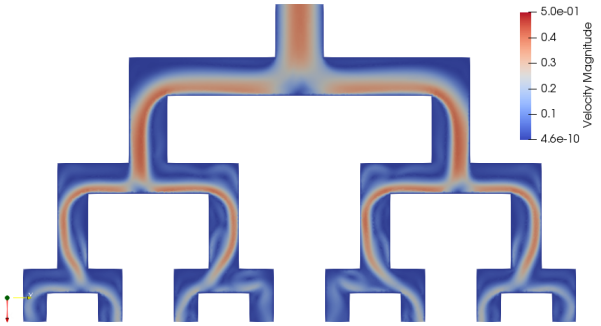

Figure 4.6: Velocity magnitude inside the manifold.

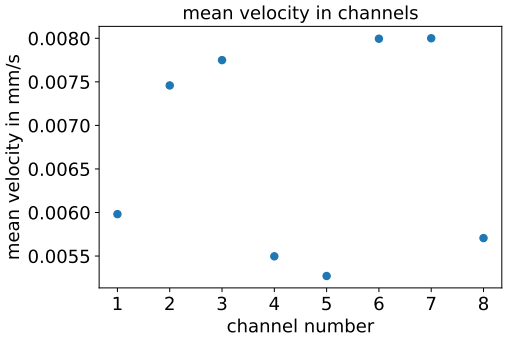

Figure 4.7: Flow rate in each channel.

4.5 Estimated production rate

We want to estimate the production rate a microfluidic droplet maker. The break-up time of a droplet is give by;

$$t_{breakup} = 2.91\sqrt{\frac{\rho R_{orifice}^3}{\sigma}} \tag{4.5}$$

hence the number of droplet per second is given by its inverse. We assume that the outer radius of the droplet is 1.5x larger than the orifice.

$$\gamma = \frac{R_{droplet}}{R_{orifice}} = 1.5 \tag{4.6}$$

and the volume per droplet is given by:

$$V_{droplet} = \frac{4}{3}\pi(\gamma R_{orifice})^3 \tag{4.7}$$

From this we can calculate the number of droplets per hour, which we can multiply by the average weight of a droplet to get the production yield in weight, which is shown below.

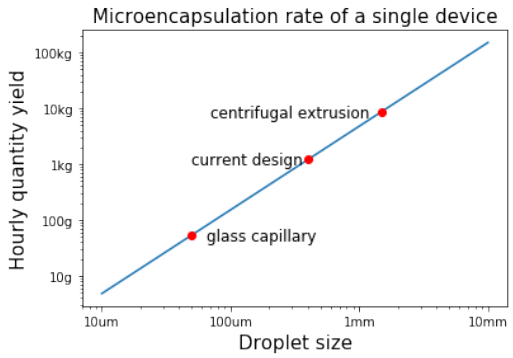

Figure 4.8: Production yield for water and oil emulsions.

4.6 Conclusion

In conclusion, we have proposed and demonstrated a sequential stacked microfluidic droplet maker, which combines scalability of surface treatment with scalability of component manufacturing. Through better control of tolerances and wedge correction during the alignment process, we believe that our approach has the potential to enable an industrial-scale microfluidic droplet maker, which is the focus of our future research.

Bibliography

[1] Benedikt Groever et al. “High-efficiency chiral meta-lens”. In: *Scientific reports* 8.1 (2018), p. 7240.

[2] M. Born and E. Wolf. *Principles of Optics: Electromagnetic Theory of Propagation, Interference and Diffraction of Light*. 2009.

[3] J. S. Tyo et al. “Review of passive imaging polarimetry for remote sensing applications”. In: *Applied Optics* 45 (2006), pp. 5453–5469.

[4] F. Snik et al. “Long-range polarimetric imaging through fog”. In: *Applied Optics* 53 (2014), pp. 3854–3865.

[5] F. Snik et al. “An overview of polarimetric sensing techniques and technology with applications to different research fields”. In: *Proc. SPIE* 20 (2014), pp. 317–330.

[6] W. Plucknett and R. Dowd. “Refraction and Polarization Properties of Binary Solutions of the Nitrotoluene Isomers with the Xylene Isomers, Chloroform and Cyclohexane”. In: *Journal of Chemical and Engineering Data* 8 (1963), pp. 207–210.

[7] J. Deuze et al. “Remote sensing of aerosols over land surfaces from Polder Adeos 1 polarized measurements”. In: *Journal of Geophysical Research: Atmospheres* 106 (2001), pp. 4913–4926.

[8] S.-S. Lin et al. “Polarization-based and specular-reflection-based noncontact latent fingerprint imaging and lifting”. In: *JOSA A* 23 (2006), pp. 2137–2153.

[9] E. Salomatina-Motts, V. Neel, and A. Yaroslavskaya. “Multimodal polarization system for imaging skin cancer”. In: *Optics and Spectroscopy* 107 (2009), pp. 884–890.

[10] B. I. Gramatikov et al. “Directional eye fixation sensor using birefringence-based foveal detection”. In: *Applied Optics* 46 (2007), pp. 1809–1818.

[11] M. Khorasaninejad et al. “Multispectral Chiral Imaging with a Meta lens”. In: *Nano Letters* 7 (2016), pp. 4595–4600.

[12] I. Hodgkinson et al. “Mueller-matrix characterization of beetle cuticle: polarized and unpolarized reflections from representative architectures”. In: *Applied Optics* 45 (2010), pp. 4558–4567.

[13] V. Sharma et al. “Structural origin of circularly polarized iridescence in jeweled beetles”. In: *Science* 325 (2009), pp. 449–451.

[14] S. Vignolini et al. “Pointillist structural color in Pollia fruit”. In: *Proceedings of the National Academy of Sciences* 109 (2012), pp. 15712–15715.

[15] B. Groever, W. T. Chen, and F. Capasso. “Meta-lens doublet in the visible”. In: *Nano Letters* 8 (2017), pp. 4902–4907.

[16] Zin Lin et al. “Topology Optimized Multi-layered Meta-optics”. In: *Physical Review Applied* 8 (2018), p. 044030.

[17] N. Yu et al. “Light Propagation with Phase Discontinuities: Generalized Laws of Reflection and Refraction”. In: *Science* 334 (2011), pp. 333–337.

[18] A. Arbabi et al. “Dielectric metasurfaces for complete control of phase and polarization with subwavelength spatial resolution and high transmission”. In: *Nature Nanotechnology* 10 (2015), pp. 937–943.

[19] M. V. Berry. “The adiabatic phase and Pancharatnam’s phase for polarized light”. In: *Journal of Modern Optics* 34 (1987), pp. 1401–1407.

[20] S. Pancharatnam. “Generalized theory of interference, and its applications”. In: *S. Proc. Indian Acad. Sci.* 44.5 (1956), pp. 247–262.

[21] M. V. Berry. “Quantal phase factors accompanying adiabatic changes”. In: *Proceedings of the Royal Society of London A: Mathematical, Physical and Engineering Science* (1984), pp. 45–47.

[22] D. Lin et al. “Dielectric gradient metasurface optical elements”. In: *Science* 345 (2014), pp. 298–302.

[23] Z. e. Bomzon, V. Kleiner, and E. Hasman. “Pancharatnam-Berry phase in space-variant polarization-state manipulations with subwavelength gratings”. In: *Optics Letters* 26 (2001), pp. 1424–1426.

[24] E. Hasman et al. “Polarization beam-splitters and optical switches based on space-variant computer-generated subwavelength quasi-periodic structures”. In: *Optics Communications* 209 (2002), pp. 45–54.

[25] E. Hasman et al. “Polarization dependent focusing lens by use of quantized Pancharatnam-Berry phase diffractive optics”. In: *Applied physics letters* 82 (2003), pp. 328–330.

[26] J. B. Mueller et al. “Metasurface polarization optics: Independent phase control of arbitrary orthogonal states of polarization”. In: *Physical Review Letters* 118 (2017), p. 113901.

[27] R. C. Devlin et al. “Arbitrary spin-to-orbital angular momentum conversion of light”. In: *Science* 358 (2017), pp. 896–901.

[28] R. C. Devlin et al. “Broadband high-efficiency dielectric metasurfaces for the visible spectrum”. In: *Proceedings of the National Academy of Sciences* 358 (2016), pp. 896–901.

[29] Benedikt Groever et al. “Substrate aberration and correction for meta-lens imaging: an analytical approach”. In: *submitted to Applied Optics* (2018).

[30] B. C. Kress and P. Meyrueis. *Applied Digital Optics: From Micro-optics to Nanophotonics*. 2009.

[31] N. Yu and F. Capasso. “Flat optics with designer metasurfaces”. In: *Nature Material* 13 (2014), pp. 139–150.

[32] Y. W. Huang et al. “Aluminum Plasmonic Multicolor Meta-Hologram”. In: *Nano Letter* 15 (2015), pp. 3122–3127.

[33] H. NS. Krishnamoorthy et al. “Topological transitions in metamaterials”. In: *Science* 336 (2012), pp. 205–209.

[34] Y. Z. Liu et al. “High-speed full analytical holographic computations for true-life scenes”. In: *Optics Express* 18 (2010), pp. 3345–3351.

[35] M. Khorasaninejad et al. “Metalenses at visible wavelengths: Diffraction-limited focusing and subwavelength resolution imaging”. In: *Science* 352 (2016), pp. 1190–1994.

[36] S.A. Bedini. “Lens making for scientific instrumentation in the seventeenth century”. In: *Applied Optics* 5 (1996), pp. 687–694.

[37] T. Stone and N. George. “Hybrid diffractive-refractive lenses and achromats”. In: *Applied Optics* 27 (1988), pp. 2960–2971.

[38] D. W. Sweeney and G. E. Sommargren. “Harmonic Diffractive Lenses”. In: *Applied Optics* 34 (1995), pp. 2469–2475.

[39] D. Faklis and G. M. Morris. “Spectral properties of multiorder diffractive lenses”. In: *Applied Optics* 34 (1995), pp. 2462–2468.

[40] F. Aieta et al. “Multiwavelength Achromatic Metasurfaces by Dispersive Phase Compensation”. In: *Science* 347 (2015), pp. 1342–1345.

[41] M. Khorasaninejad et al. “Achromatic Meta-lens over 60 nm Bandwidth in the Visible and Metalens with Reverse Chromatic Dispersion”. In: *Nano Letter* 17 (2017), pp. 1819–1824.

[42] S. Wang et al. “Broadband achromatic optical metasurface devices”. In: *Nature Communication* 8 (2017).

[43] Y. Soskind. “Field guide to diffractive optics”. In: *SPIE Press* (2011).

[44] G. J. Swanson. “Binary optics technology: The theory and design of multi-level diffractive optical elements”. In: *Report, DTIC Document* (1989).

[45] M. B. Stern. “Binary optics: A VLSI-based microoptics technology”. In: *Microelectron. Eng* 32 (1996), pp. 369–388.

[46] M. Khorasaninejad et al. “Achromatic Metasurface Lens at Telecommunication Wavelengths”. In: *Nano Letter* 15 (2015), pp. 5358–5362.

[47] M. Khorasaninejad et al. “Super-Dispersive Off-Axis Meta-lenses for Compact High Resolution. spectroscopy”. In: *Nano Letter* 16 (2016), pp. 3732–3737.

[48] A. Arbabi et al. “Subwavelength-thick lenses with high numerical apertures and large efficiency based on high-contrast transmitarrays”. In: *BioTechniques* 33 (2002), pp. 772–781.

[49] K. Esswein. *Attachment of microscope objectives*. US4515439 A. 1985.

[50] M. Abramowitz et al. “Basic principles of microscope objectives”. In: *BioTechniques* 33 (2002), pp. 772–781.

[51] T. Ito and S. Okazaki. “Pushing the limits of lithography”. In: *Nature* 406 (2000), pp. 1027–1031.

[52] F. Aieta et al. “Aberration-Free Ultrathin Flat Lenses and Axicons at Telecom Wavelengths Based on Plasmonic Metasurfaces”. In: *Nano Letter* 12 (2012), pp. 4932–4936.

[53] F. Aieta et al. “Aberrations of flat lenses and aplanatic metasurfaces”. In: *Optics Express* 21 (2013), pp. 31530–31539.

[54] B. Groever, W.T. Chen, and F. Capasso. “Meta-lens doublet in the visible”. In: *Nano Letter* 8 (2017), pp. 4902–4907.

[55] A. Arbabi et al. “Miniature optical planar camera based on a wide-angle metasurface doublet corrected for monochromatic aberrations”. In: *Nature Communication* 7 (2016), p. 13682.

[56] Florian Bociort. “Optical system optimization”. In: *Encyclopedia Of Optical Engineering* 2 (2003), pp. 1843–1850.

[57] M. Peschka et al. *Handbook of Optical Systems: Vol. 3. Aberration Theory and Correction of Optical Systems*. 2007.

[58] A. She et al. “Large area electrically tunable lenses based on metasurfaces and dielectric elastomer actuators”. In: *Optics express* 26 (2018), pp. 1573–1585.

[59] B. Groever. *GiveMeFV.m*. `https://osapublishing.figshare.com/s/00a3cb6a9f945b7d7d56`. Accessed: 2017-10-23. 2017.

[60] S. Sun et al. “Gradient-index meta-surfaces as a bridge linking propagating waves and surface waves”. In: *Nature Material* 11 (2012), pp. 426–431.

[61] S. Sun et al. “High-Efficiency Broadband Anomalous Reflection by Gradient Meta-Surfaces”. In: *Nano Letter* 12 (2012), pp. 6223–6229.

[62] B. C. Kress and P. Meyrueis. *Applied Digital Optics: From Micro-optics to Nanophotonics*. 2009.

[63] Z. Lin et al. “Topology optimized multi-layered meta-optics”. In: *Physical Review Applied* 9 (2018).

[64] W. J. Smith. *Modern optical engineering*. 1966.

[65] W. T. Chen et al. “Immersion Meta-lenses at Visible Wavelengths for Nanoscale Imaging”. In: *Nano Letter* 17 (2017), pp. 3188–3194.

[66] R. Kingslake. *A history of the photographic lens*. 1989.

[67] Henry C King. *The history of the telescope*. Courier Corporation, 1955. ISBN: 0486432653.

[68] Francesco Aieta et al. “Aberration-Free Ultrathin Flat Lenses and Axicons at Telecom Wavelengths Based on Plasmonic Metasurfaces”. In: *Nano Lett.* 12.9 (2012), pp. 4932–4936.

[69] Herbert Gross et al. *Handbook of Optical Systems: Vol. 3. Aberration Theory and Correction of Optical Systems.* 2007.

[70] Marija Strojnik et al. *Handbook of Optical Engineering*. Marcel Dekker New York, 2001.

[71] Alexander V Kildishev, Alexandra Boltasseva, and Vladimir M Shalaev. "Planar photonics with metasurfaces". In: *Science* 339.6125 (2013).

[72] Wei Ting Chen et al. "Integrated plasmonic metasurfaces for spectropolarimetry". In: *Nanotechnology* 27.22 (2016), p. 224002.

[73] Wei Ting Chen et al. "High-Efficiency Broadband Meta-Hologram with Polarization-Controlled Dual Images". In: *Nano Lett.* 14.1 (2014), pp. 225–230.

[74] Benedikt Groever, Barmak Heshmat, and Ramesh Raskar. "Tyndall Windows: Tunable Scattering of Disordered Solid-Liquid Matching Mixtures". In: *ACS Photonics* 3.6 (2016), pp. 930–935.

[75] Jiaming Hao et al. "Manipulating electromagnetic wave polarizations by anisotropic metamaterials". In: *Phys. Rev. Lett.* 99.6 (2007), p. 063908.

[76] Lingling Huang et al. "Dispersionless phase discontinuities for controlling light propagation". In: *Nano Lett.* 12.11 (2012), pp. 5750–5755.

[77] Satoshi Kawata et al. "Finer features for functional microdevices". In: *Nature* 412.6848 (2001), pp. 697–698.

[78] Xiaoze Liu et al. "Strong light-matter coupling in two-dimensional atomic crystals". In: *Nat. Photonics* 9.1 (2015), pp. 30–34.

[79] Boris Luk'yanchuk et al. "The Fano resonance in plasmonic nanostructures and metamaterials". In: *Nat. Mater.* 9.9 (2010), pp. 707–715.

[80] Jason Valentine et al. "Three-dimensional optical metamaterial with a negative refractive index". In: *Nature* 455.7211 (2008), pp. 376–379.

[81] E Plum et al. "Metamaterial with negative index due to chirality". In: *Phys. Rev. B* 79.3 (2009), p. 035407.

[82] Wei Ting Chen et al. "Generation of Wavelength-independent Sub-wavelength Bessel Beams using Metasurfaces". In: *Light: Sci. Appl.* 14 (2016).

[83] Edward TF Rogers et al. "A super-oscillatory lens optical microscope for subwavelength imaging". In: *Nat. Mater.* 11.5 (2012), pp. 432–435.

[84] B Wood, JB Pendry, and DP Tsai. "Directed subwavelength imaging using a layered metal-dielectric system". In: *Phys. Rev. B* 74.11 (2006), pp. 115–116.

[85] Dale A Buralli and G Michael Morris. “Design of a wide field diffractive landscape lens”. In: *Applied optics* 28.18 (1989), pp. 3950–3959.

[86] TJ Johnson. *Method for making replica contour block masters for producing schmidt corrector plates*. US Patent 3, 837, 124. 1974.

[87] TJ Johnson. *Method for making Schmidt Corrector Lenses*. US Patent 3, 889, 431. 1975.

[88] `https://www.thorlabs.com/newgrouppage9.cfm?objectgroup_id=9895`. Accessed: 2017-10-23. 2017.

[89] Jiao Lin et al. “Polarization-controlled tunable directional coupling of surface plasmon polaritons”. In: *Science* 340.6130 (2013), pp. 331–334.

[90] Mohammadreza Khorasaninejad et al. “Achromatic Metalens over 60 nm Bandwidth in the Visible and Metalens with Reverse Chromatic Dispersion”. In: *Nano Letter* 17.3 (2017), pp. 1819–1824.

[91] Sujit S Datta et al. “25th anniversary article: Double emulsion templated solid microcapsules: Mechanics and controlled release”. In: *Advanced Materials* 26.14 (2014), pp. 2205–2218.

[92] Nissim Garti and D Julian McClements. *Encapsulation technologies and delivery systems for food ingredients and nutraceuticals*. Elsevier, 2012.

[93] Tae Yong Lee et al. “Microfluidic production of multiple emulsions and functional microcapsules”. In: *Lab on a Chip* 16.18 (2016), pp. 3415–3440.

[94] Sara J Risch. “Encapsulation of flavors by extrusion”. In: *ACS Symposium series American Chemical Society*.

[95] Wade Schlameus. “Centrifugal extrusion encapsulation”. In: ACS Publications, 1995.

[96] Bernard F. Gibbs et al. “Encapsulation in the food industry: a review”. In: *International journal of food sciences and nutrition* 50.3 (1999), pp. 213–224.

[97] AS Utada et al. “Dripping, jetting, drops, and wetting: The magic of microfluidics”. In: *Mrs Bulletin* 32.9 (2007), pp. 702–708.

[98] AS Utada et al. “Monodisperse double emulsions generated from a microcapillary device”. In: *Science* 308.5721 (2005), pp. 537–541.

[99] PJ Simpson et al. “Intrinsic tolerance of Bifidobacterium species to heat and oxygen and survival following spray drying and storage”. In: *Journal of Applied Microbiology* 99.3 (2005), pp. 493–501.

[100] Song Huang et al. “Spray drying of probiotics and other food-grade bacteria: A review”. In: *Trends in food science & technology* 63 (2017), pp. 1–17.

[101] Elad Stolovicki, Roy Ziblat, and David A Weitz. “Throughput enhancement of parallel step emulsifier devices by shear-free and efficient nozzle clearance”. In: *Lab on a Chip* 18.1 (2018), pp. 132–138.

[102] Alessandro Ofner et al. “High Throughput Step Emulsification for the Production of Functional Materials Using a Glass Microfluidic Device”. In: *Macromolecular Chemistry and Physics* 218.2 (2017).

[103] ML Eggersdorfer et al. “Tandem emulsification for high-throughput production of double emulsions”. In: *Lab on a Chip* 17.5 (2017).

[104] Mark B Romanowsky et al. “High throughput production of single core double emulsions in a parallelized microfluidic device”. In: *Lab on a Chip* 12.4 (2012), pp. 802–807.

[105] LR Arriaga, E Amstad, and DA Weitz. “Scalable single-step microfluidic production of single-core double emulsions with ultra-thin shells”. In: *Lab on a Chip* 15.16 (2015), pp. 3335–3340.

[106] Brandon L Thompson et al. “Inexpensive, rapid prototyping of microfluidic devices using overhead transparencies and a laser print, cut and laminate fabrication method”. In: *Nature protocols* 10.6 (2015), p. 875.

[107] Richard Novak, Carlos F Ng, and Donald E Ingber. “Rapid Prototyping of Thermoplastic Microfluidic Devices”. In: *Cell - Based Microarrays*. Springer, 2018, pp. 161–170.

[108] Richard Novak, Navpreet Ranu, and Richard A Mathies. “Rapid fabrication of nickel molds for prototyping embossed plastic microfluidic devices”. In: *Lab on a Chip* 13.8 (2013), pp. 1468–1471.

[109] S Ali Aghvami et al. “Rapid prototyping of cyclic olefin copolymer (COC) microfluidic devices”. In: *Sensors and Actuators B: Chemical* 247 (2017), pp. 940–949.

[110] Berengere Guignon, Albert Duquenoy, and Elisabeth D Dumoulin. “Fluid bed encapsulation of particles: principles and practice”. In: *Drying Technology* 20.2 (2002), pp. 419–447.

[111] Gary Bradski and Adrian Kaehler. *Learning OpenCV: Computer vision with the OpenCV library*. " O'Reilly Media, Inc.", 2008.

[112] Muhammad Iqbal et al. "Double emulsion solvent evaporation techniques used for drug encapsulation". In: *International journal of pharmaceutics* 496.2 (2015), pp. 173–190.

[113] Eric Jones, Travis Oliphant, and Pearu Peterson. "SciPy: Open source scientific tools for Python". In: (2001).

[114] VH Holsinger et al. "A cost analysis of encapsulated spray-dried milk fat". In: *Journal of dairy science* 83.10 (2000), pp. 2361–2365.